

1 **Drug-induced epigenomic plasticity reprograms circadian rhythm regulation to**
2 **drive prostate cancer towards androgen-independence**

3 Simon Linder^{1,*}, Marlous Hoogstraat^{1,2,*}, Suzan Stelloo¹, Karianne Schuurman¹, Hilda de Barros³, Maartje
4 Alkemade⁴, Joyce Sanders⁵, Yongsoo Kim⁶, Elise Bekers⁵, Jeroen de Jong⁵, Roelof J.C. Kluin⁷, Claudia
5 Giambartolomei^{8,9}, Ji-Heui Seo¹⁰, Bogdan Pasaniuc^{8,9}, Amina Zoubeidi^{11,12}, Matthew L. Freedman^{10,13},
6 Lodewyk F.A. Wessels^{2,14}, Lisa M. Butler^{15,16}, Nathan A. Lack^{12,17,18}, Henk van der Poel^{3,#}, Andries M.
7 Bergman^{19,20,#} and Wilbert Zwart^{1,21,#}

8

9 ¹ Division of Oncogenomics, Oncode Institute, The Netherlands Cancer Institute, Amsterdam, 1066 CX,
10 The Netherlands.

11 ² Division of Molecular Carcinogenesis, Oncode Institute, The Netherlands Cancer Institute, Amsterdam,
12 1066 CX, The Netherlands.

13 ³ Division of Urology, The Netherlands Cancer Institute, Amsterdam, 1066 CX, The Netherlands.

14 ⁴ Core Facility Molecular Pathology & Biobanking, The Netherlands Cancer Institute, Amsterdam, 1066 CX,
15 The Netherlands.

16 ⁵ Division of Pathology, The Netherlands Cancer Institute, Amsterdam, 1066 CX, The Netherlands.

17 ⁶ Department of Pathology, Amsterdam UMC, Cancer Center Amsterdam, Amsterdam, 1181 HV, The
18 Netherlands.

19 ⁷ Genomics Core Facility, The Netherlands Cancer Institute, Amsterdam, 1066 CX, The Netherlands.

20 ⁸ Department of Pathology and Laboratory Medicine, David Geffen School of Medicine, University of
21 California, Los Angeles, Los Angeles, CA 90095, USA.

22 ⁹ Department of Human Genetics, David Geffen School of Medicine, University of California, Los Angeles,
23 Los Angeles, CA 90095, USA.

24 ¹⁰ Department of Medical Oncology, Dana-Farber Cancer Institute, Harvard Medical School, Boston, MA
25 02215, USA.

26 ¹¹ Department of Urologic Sciences, University of British Columbia, Vancouver, V5Z 1M9 BC, Canada.

27 ¹² Vancouver Prostate Centre, University of British Columbia, Vancouver, V6H 3Z6 BC, Canada.

28 ¹³ The Eli and Edythe L. Broad Institute, Cambridge, MA 02142, USA.

29 ¹⁴ Faculty of EEMCS, Delft University of Technology, Delft, 2628 CD, The Netherlands.

30 ¹⁵ Freemasons Centre for Male Health and Wellbeing, Adelaide Medical School, University of Adelaide,
31 Adelaide, SA 5005, Australia.

32 ¹⁶ South Australian Health and Medical Research Institute, Adelaide, SA 5000, Australia.

33 ¹⁷ School of Medicine, Koç University, Istanbul, 34450, Turkey.

34 ¹⁸ Koç University Research Centre for Translational Medicine (KUTTAM), Koç University, Istanbul, 34450,
35 Turkey.

36 ¹⁹ Division of Oncogenomics, The Netherlands Cancer Institute, Amsterdam, 1066 CX, The Netherlands.

37 ²⁰ Division of Medical Oncology, The Netherlands Cancer Institute, Amsterdam, 1066 CX, The Netherlands.

38 ²¹ Laboratory of Chemical Biology and Institute for Complex Molecular Systems, Department of Biomedical
39 Engineering, Eindhoven University of Technology, Eindhoven, 5612 AZ, The Netherlands.

40

41 * S. Linder and M. Hoogstraat contributed equally to this article.

42

43 # **Corresponding Authors:** Henk van der Poel, Andries M. Bergman and Wilbert Zwart; The Netherlands
44 Cancer Institute, Plesmanlaan 121, 1066 CX Amsterdam, The Netherlands. Phone: +31 20 512 2101; E-
45 mail: h.vd.poel@nki.nl; a.bergman@nki.nl; w.zwart@nki.nl

46

47 **Running Title:** Drug-induced epigenomic plasticity drives PCa cell survival

48 **Abstract**

49 In prostate cancer, androgen receptor (AR)-targeting agents are very effective in various stages of the
50 disease. However, therapy resistance inevitably occurs and little is known about how tumor cells adapt to
51 bypass AR suppression. Here, we performed integrative multi-omics analyses on tissues isolated before
52 and after 3 months of AR-targeting enzalutamide monotherapy from high-risk prostate cancer patients
53 enrolled in a neoadjuvant clinical trial. Transcriptomic analyses demonstrated that AR inhibition drove
54 tumors towards a neuroendocrine-like disease state. In addition, epigenomic profiling revealed massive
55 enzalutamide-induced reprogramming of pioneer factor FOXA1 – from inactive chromatin binding sites
56 towards active *cis*-regulatory elements that dictate pro-survival signals. Notably, treatment-induced FOXA1
57 sites were enriched for the circadian rhythm core component ARNTL. Post-treatment ARNTL levels
58 associated with poor outcome, and ARNTL suppression decreased cell growth *in vitro*. Our data highlight
59 a remarkable cis-tromic plasticity of FOXA1 following AR-targeted therapy, and revealed an acquired
60 dependency on circadian regulator ARNTL, a novel candidate therapeutic target.

61

62 **Significance**

63 Understanding how prostate cancer cells adapt to AR-targeted interventions is critical for identifying
64 novel drug targets to improve the clinical management of treatment-resistant disease. Our study revealed
65 an enzalutamide-induced epigenetic plasticity towards pro-survival signaling, and uncovered circadian
66 regulator ARNTL as an acquired vulnerability after AR inhibition, presenting a novel clinical lead for
67 therapeutic development.

68

69 **Keywords**

70 Prostate cancer, neoadjuvant clinical trial, Androgen Receptor, enzalutamide, epigenetic plasticity,
71 FOXA1, circadian rhythm, ARNTL

72

73 **Introduction**

74 Hormonal ablation is the mainstay treatment for patients with metastatic prostate cancer (PCa), ever
75 since the direct critical connection between androgens and prostate tumor progression was first described

76 (1). The androgen receptor (AR) is the key driver of PCa development and progression, and multiple
77 therapeutic strategies have been developed over the years to effectively block the activity of this hormone-
78 driven transcription factor. Upon androgen binding, AR associates with the chromatin at distal *cis*-regulatory
79 enhancer elements, where it regulates the expression of genes through long-range chromatin interactions
80 in three-dimensional genomic space (2,3). AR does not operate in isolation, but rather recruits a large
81 spectrum of coregulators and other transcription factors to promote expression of genes that drive cancer
82 cell proliferation (4). Critical AR interactors in the transcription complex are HOXB13 and FOXA1, which
83 are both upregulated in primary PCa (4-6) and demarcate enhancers that drive not only primary
84 tumorigenesis but also metastatic disease progression (7). Mechanistically, FOXA1 acts as a pioneer
85 factor, rendering the chromatin accessible for AR to bind (8-11). *FOXA1* is frequently mutated in PCa (12-
86 16) which was shown to alter its pioneering capacities, perturb luminal epithelial differentiation programs,
87 and promote tumor growth, further highlighting the critical role of FOXA1 in human prostate tumors (17,18).
88 Most patients are diagnosed with organ-confined PCa, which can potentially be cured through locoregional
89 therapies, such as surgery (radical prostatectomy), radiotherapy and/or brachytherapy (19). However,
90 approximately 30% of these patients experience a biochemical recurrence (BCR) – a rise in prostate-
91 specific antigen (PSA) serum levels – indicating PCa relapse (20). At this stage of the disease, suppression
92 of androgen production is a commonly applied therapeutic intervention that can delay further cancer
93 progression for years (21,22). Nevertheless, the development of resistance to androgen deprivation is
94 inevitable, resulting in castration-resistant prostate cancer (CRPC) for which there is no cure (23). Most
95 CRPC tumors acquired molecular features that enable active AR signaling despite low circulating androgen
96 levels, a finding that led to the development of several highly effective AR-targeted therapies. Enzalutamide
97 (ENZ) is one of the most frequently used AR-targeting agents, which functions through a combined
98 mechanism of blocked AR nuclear import, diminished AR chromatin binding and decreased transcription
99 complex formation, effectively impairing AR-driven PCa growth (24). ENZ's potent anti-tumor activity has
100 been demonstrated in multiple clinical trials, which led to its FDA approval in various PCa disease stages
101 – from metastatic CRPC (25,26), to metastatic hormone-sensitive (27), and even non-metastatic CRPC
102 (28) – illustrating how AR-targeted therapies are being progressively introduced earlier in clinical practice.
103 A clinical benefit of ENZ monotherapy as a neoadjuvant treatment prior to prostatectomy for patients with

104 localized disease, has not been established. Although effective, resistance to AR pathway inhibition will
105 ultimately develop, and the management of advanced PCa with this acquired resistance remains a major
106 clinical challenge, especially since the underlying mechanisms are still not fully elucidated (29). Therefore,
107 furthering our understanding of how ENZ affects PCa biology may lead to the identification of acquired
108 cellular vulnerabilities that could be therapeutically exploited.

109 To study global drug-induced transcriptional and epigenetic plasticity in human prostate tumors and identify
110 cellular adaptation mechanisms to evade drug treatment, we designed a phase 2 clinical trial to perform
111 multi-omics studies in pre- and post-treatment samples from high-risk localized PCa patients, treated with
112 neoadjuvant ENZ monotherapy. We identified transcriptional reprogramming after treatment, with
113 deactivation of AR signaling and an activation of cell plasticity with neuroendocrine (NE)-like features upon
114 3 months of AR suppression. Post treatment, these tumors harbored a distinct set of 1,430 *de novo*
115 occupied FOXA1-positive *cis*-regulatory elements, positive for – yet independent of – AR activity, which are
116 dictated by circadian clock core regulator ARNTL to drive tumor cell proliferation instead. Using ARNTL
117 knockdown experiments we could further enhance ENZ sensitivity in cell line models, revealing an
118 unexpected biological interplay between hormonal resistance and circadian rhythm regulation, and
119 identifying a novel highly promising candidate drug target in the clinical management of primary high-risk
120 PCa.

121

122 **Results**

123 **Neoadjuvant ENZ therapy for patients with high-risk localized PCa**

124 To study how early ENZ intervention affects prostate tumor biology in a non-castrate environment, we
125 performed integrative multi-omics analyses as part of a single-arm, open-label phase 2 clinical trial: the
126 DARANA study (Dynamics of Androgen Receptor Genomics and Transcriptomics After Neoadjuvant
127 Androgen Ablation; ClinicalTrials.gov number, NCT03297385). In this trial, 56 men with primary high-risk
128 (Gleason score ≥ 7) PCa were enrolled (**Fig. 1A**). Patient demographics and disease characteristics are
129 summarized in **Table 1**, and clinical outcomes of this study are discussed in **Supplementary Data**
130 (**Supplementary Fig. S1; Supplementary Table S1**). Prior to ENZ therapy, magnetic resonance imaging
131 (MRI)-guided core needle tumor biopsies were taken – hereafter referred to as the pre-treatment setting.

132 Subsequently, patients received neoadjuvant ENZ treatment (160 mg/day) without androgen deprivation
133 therapy for three months, followed by robotic-assisted laparoscopic prostatectomy. Based on baseline MRI
134 information and palpation, additional tumor-targeted core needle biopsies were taken *ex vivo* – representing
135 the post-treatment setting. This pre- and post-treatment sampling allowed us to study the epigenetic,
136 genomic, transcriptomic and proteomic effects of neoadjuvant ENZ therapy in individual patients (**Fig. 1A**).
137 We generated chromatin immunoprecipitation (ChIP-seq) profiles of the prostate cancer drivers AR and
138 FOXA1, as well as the histone modification H3K27ac before and after ENZ treatment, and integrated these
139 cistromic findings with pre- and post-treatment gene expression (RNA-seq), copy number (CNV-seq) and
140 immunohistochemistry (IHC) data from the same tumors. Stringent quality control (QC) analyses were
141 performed on all data streams (**Supplementary Fig. S1B**), and the following number of samples passed
142 all QC measures (**Fig. 1B**): AR ChIP-seq (pre: n=10; post: n=12), FOXA1 ChIP-seq (pre: n=17; post: n=17),
143 H3K27ac ChIP-seq (pre: n=24; post: n=23), CNV-seq (pre: n=24; post: n=24), RNA-seq (pre: n=42; post:
144 n=52) and IHC (post: n=51).
145 Collectively, we performed integrative multi-omics analyses as part of a clinical trial that enabled us to
146 examine ENZ-induced oncogenomic changes to identify early epigenetic steps in treatment response, but
147 also therapy-induced resistance.

148

149 **Characterization of tissue ChIP-seq data**

150 To assess how neoadjuvant ENZ treatment affects the *cis*-regulatory landscape in primary PCa, we
151 generated human tumor ChIP-seq profiles for the transcription factors AR and FOXA1, along with the active
152 enhancer/promoter histone mark H3K27ac before and after neoadjuvant intervention. ChIP-seq quality
153 metrics are summarized in **Supplementary Fig. S2** and **Supplementary Table S2**. Visual inspection at
154 known AR target genes showed high-quality data for all ChIP-factors in both clinical settings (**Fig. 2A**). On
155 a genome-wide scale, the H3K27ac ChIP-seq profiles were highly distinct from the transcription factors
156 (TFs) and divided the samples into two main clusters irrespective of their treatment status (**Fig. 2B and**
157 **2C**). Notably, AR and FOXA1 ChIP-seq datasets were intermingled in the clustering analysis, suggesting
158 largely comparable binding profiles which is in line with FOXA1's role as a canonical AR pioneer factor
159 (**Supplementary Fig. S3**) (5,30). As described previously (31), highest Pearson correlation was found

160 between H3K27ac samples, indicating comparable histone acetylation profiles among primary PCa
161 samples (**Fig. 2B**; **Supplementary Fig. S3**). Much greater heterogeneity in chromatin binding was
162 observed for the TFs AR and FOXA1, which is further supported by the steep decrease in the number of
163 overlapping AR and FOXA1 peaks with increasing number of samples compared to H3K27ac (**Fig. 2D**;
164 **Supplementary Fig. S3**). In order to maintain the high-confidence peaks that have been reproducibly
165 identified in multiple patients without losing too much binding site heterogeneity between samples, we
166 decided to generate consensus peaksets. To this end, we only considered binding sites that were present
167 in at least 3 out of 22 AR samples, 7 out of 34 FOXA1 samples and 13 out of 47 H3K27ac samples, which
168 corresponds to ~25% of all binding sites identified for each factor (**Fig. 2D**). Genomic distribution analyses
169 of these consensus sites revealed distinct enrichments for annotated genomic regions: While AR and
170 FOXA1 were almost exclusively found at intronic and distal intergenic regions, H3K27ac peaks were also
171 enriched at promoters (**Fig. 2E**), which is in line with previously published genomic distributions of AR
172 (5,31), FOXA1 (5,9), and H3K27ac (31,32). In addition, motif enrichment analyses at AR and FOXA1
173 consensus peaks identified, as expected, androgen and Forkhead response elements among the top-
174 ranked motifs, respectively (**Fig. 2F**).

175 Taken together, we generated multiple high-quality tissue ChIP-seq data streams that now allowed us to
176 study ENZ-induced changes in primary PCa patients.

177

178 **ENZ treatment enriches for newly acquired FOXA1-bound regulatory regions**

179 To identify ENZ-induced TF reprogramming and epigenetic changes, we performed differential binding
180 analyses comparing the pre- and post-treatment tissue ChIP-seq samples. Therefore, we first ran
181 occupancy-based unsupervised principal component analyses (PCA) to detect whether ENZ treatment led
182 to differences in TF chromatin binding. While the sample size of the AR ChIP-seq data stream was not
183 sufficient to observe significant differences in peak occupancy pre- versus post-treatment (**Supplementary**
184 **Fig. S4A**), the FOXA1 data did show such differences, with a clear separation of pre- and post-treatment
185 FOXA1 samples in the second principal component (**Fig. 3A**). Subsequent supervised analysis (pre vs.
186 post) revealed a total of 1,905 genomic regions (475 pre-enriched, 1,430 post-enriched; **Supplementary**
187 **Table S3**) that showed significant differential FOXA1 binding between both clinical settings (FDR < 0.05;

188 **Fig. 3B and 3C; Supplementary Fig. S4B and S4C**). Further characterization of these differential FOXA1
189 regions showed that both sets of binding sites were still preferentially located in intronic and distal intergenic
190 regions (with a slight enrichment for promoters at the post-enriched sites; **Supplementary Fig. S4D**). In
191 addition, Forkhead domain family motifs were the top enriched motifs at both pre- and post-enriched sites,
192 illustrating that treatment does not alter FOXA1 motif preference and still occupies canonical FOXA1
193 binding sites (**Supplementary Fig. S4E**).

194 To examine whether structural variations are underlying these differential FOXA1 binding events, we
195 performed CNV-seq on the same tumor specimens and then projected onto the differential FOXA1
196 cistromics the structural copy-number data. These analyses revealed a comparable level of CNV at pre-
197 and post-treatment enriched FOXA1 sites before and after ENZ treatment, with an overall trend towards
198 less CNV upon treatment (**Supplementary Fig. S5A-S5C**). However, in none of the matched sample pairs
199 (pre and post CNV-seq, and FOXA1 ChIP-seq; n=15) a strong correlation between copy number difference
200 and ChIP-seq signal difference was observed ($R = 0.11$; **Supplementary Fig. S5D**). In total, at only 44 out
201 of 1,905 differential FOXA1 binding sites (< 2.5%), we observed copy number differences between post-
202 and pre-treatment samples that could potentially explain binding site occupancy in 3 or more patients,
203 indicating that the vast majority of these differential binding events is based on treatment-induced
204 transcription factor reprogramming, rather than structural variation (**Supplementary Fig. S5E**).

205 As FOXA1 dictates AR chromatin binding capacity (5), epigenetic plasticity of FOXA1 induced by treatment
206 may be associated with alterations in the AR cistrome. To assess this, and to explore the epigenetic
207 landscape surrounding the differentially bound FOXA1 regions, we compared the ChIP-seq signal of all
208 three factors (AR, FOXA1, H3K27ac) at differential (pre- / post-enriched) and consensus (shared by ≥ 30
209 patients; n=338) FOXA1 sites before and after ENZ therapy. While the FOXA1 ChIP-seq signal was highest
210 at consensus binding sites, the pre- and post-treatment enriched regions followed the expected trend and
211 showed significantly higher signal in the corresponding settings (**Fig. 3D**). Notably, we also observed less
212 binding of FOXA1 to consensus sites when treated with ENZ, although the differences are much milder
213 compared to the effects seen at pre-enriched FOXA1 sites ($P_{adj} = 3.62 \times 10^{-22}$ at consensus vs. $3.76 \times 10^{-$
214 ¹³⁰ at pre-enriched sites, Mann-Whitney U-test; **Fig. 3D; Supplementary Fig. S6A**). This could possibly be
215 explained by decreased FOXA1 gene expression levels upon ENZ treatment (**Supplementary Fig. S6B**).

216 The AR ChIP-seq signal followed the same patterns as observed for FOXA1, suggesting that relocated
217 FOXA1 upon treatment functionally drives alterations in the AR cistrome (**Fig. 3D**). Unexpectedly, the pre-
218 enriched FOXA1 sites were completely devoid of any H3K27ac signal in both pre- and post-treatment
219 samples, while the post-enriched counterparts were positive for this active enhancer/promoter mark with a
220 significant increase post-ENZ ($P_{adj} = 5.59 \times 10^{-4}$, Mann-Whitney U-test; **Fig. 3D; Supplementary Fig. S6C**
221 **and S6D**), suggesting that pre-ENZ FOXA1 sites are inactive. To validate these observations in an
222 independent cohort, we analyzed previously published AR (n=87), H3K27ac (n=92) and H3K27me3 (n=76)
223 ChIP-seq data from a cohort of 100 primary treatment-naïve PCa samples (31). Supporting our previous
224 analyses, the vast majority of post-enriched FOXA1 sites were H3K27ac-positive and their histone
225 acetylation status positively correlated with AR binding ($R = 0.78$) (**Fig. 3E; Supplementary Fig. S6E**). The
226 pre-enriched FOXA1 sites, however, were again H3K27ac-negative, while the repressive histone
227 modification H3K27me3 was present, which further points towards an inactive epigenetic state of these
228 regulatory regions (**Fig. 3E**).

229 Recently, we reported that prostate cancers can reactivate developmental programs during metastatic
230 progression (7). These sentinel enhancers appeared to be premarked by FOXA1 from prostate gland
231 development, and albeit inactive in normal and primary tumor specimens, the sites get reactivated by AR
232 during metastatic outgrowth. Given the inactivity of the pre-enriched FOXA1 sites, we hypothesized that
233 FOXA1 might be decommissioned at such developmental enhancers prior to hormonal intervention. To test
234 this, we overlapped the differential FOXA1 binding sites with the metastasis-specific AR binding sites (met-
235 ARBS; n=17,655), which revealed a strong enrichment for these developmental regulatory elements at pre-
236 treatment FOXA1 sites ($P = 2.13 \times 10^{-16}$, Fisher's exact test; **Supplementary Fig. S6F**). But are the inactive
237 pre-enriched FOXA1 sites solely epigenetically suppressed, or are these regions intrinsically incapable of
238 being active in this cellular context? To address this question and to further elucidate the role of AR at these
239 differentially bound FOXA1 sites, we integrated our tissue ChIP-seq findings with previously identified
240 tumor-specific AR binding sites (n=3,230) (5) that were functionally characterized using Self-Transcribing
241 Active Regulatory Regions sequencing (STARR-seq), a massive parallel reporter assay to systematically
242 annotate intrinsic enhancer activity (33). With this, three distinct classes of AR binding sites (ARBS) were
243 identified (**Supplementary Table S4**): enhancers that were active regardless of AR stimulation

244 (constitutively active; n=465), ARBS with no significant enhancer activity (inactive; n=2,479) and inducible
245 AR enhancers that increase activity upon androgen treatment (inducible; n=286). Interestingly, we found
246 that post-treatment FOXA1 sites were enriched for constitutively active ARBS, which further supports the
247 high enhancer activity and H3K27ac positivity observed at these sites, but also illustrates that this activity
248 is constitutive and AR-independent (**Fig. 3F**). Consistent with our postulated inactivity of the pre-treatment
249 enriched FOXA1 sites, these regions overlapped highly significantly with inactive ARBS ($P = 8.60 \times 10^{-9}$,
250 Fisher's exact test), which implies that these DNA elements are intrinsically inactive and incapable to act
251 as functional enhancers, and possibly explains why these AR-bound sites did not show active regulatory
252 marks (**Fig. 3E and 3F**). As no enrichment of our differential FOXA1 sites was observed with inducible
253 ARBS (Pre-enriched: 4/475; Post-enriched: 2/1,430), these data further support a conclusion that AR itself
254 is not a driver at FOXA1 sites that are differentially occupied after ENZ exposure in patients.

255 Overall, these results suggest that prior to hormonal intervention, FOXA1 is decommissioned at inactive
256 developmental enhancer elements, which based on their primary DNA sequence are intrinsically incapable
257 of being active – at least in the tested hormone-sensitive disease setting. However, upon ENZ treatment,
258 FOXA1 gets reprogrammed to highly active *cis*-regulatory regions, which act in an AR-independent manner.

259

260 **Transcriptional rewiring upon neoadjuvant ENZ**

261 Having assessed the cistromic and epigenomic changes in response to neoadjuvant ENZ, we next
262 determined how transcriptional programs were affected by this hormonal intervention. Principal component
263 analysis (PCA) across both treatment states revealed that three months of ENZ therapy has a major effect
264 on global gene expression profiles (**Fig. 4A**). Subsequently, we performed differential gene expression
265 analysis, in which we compared pre- and post-treatment RNA-seq samples. Gene set enrichment analysis
266 (GSEA) showed that AR signaling, along with mitosis and MYC signals, was strongly decreased upon
267 treatment (**Fig. 4B and C; Supplementary Fig. S7A**). Since ENZ blocks the AR signaling axis, we analyzed
268 the androgen-response pathway in more detail, which revealed a strong downregulation of AR target genes
269 in almost every patient (**Fig. 4D**). In contrast to this, TNF α signaling, IFN- γ response and epithelial-
270 mesenchymal transition (EMT) signals were most upregulated (**Fig. 4B; Supplementary Fig. S7B**).

271 Previously, we identified three distinct subtypes of primary treatment-naïve PCa (31), which we named
272 Cluster 1-3 (Cl1-3). While Cl1 and Cl2 were mainly dominated by their ERG fusion status – with Cl1
273 expressing high ERG levels (ERG fusion-positive) and Cl2 expressing low ERG levels (ERG fusion-
274 negative) – Cl3 was enriched for neuroendocrine (NE)-like features, including low AR activity and a high
275 NE gene expression score. To assess the impact of neoadjuvant ENZ therapy on these PCa subtypes, we
276 performed unsupervised hierarchical clustering in the pre- and post-treatment setting using the originally
277 identified top 100 most differentially expressed genes per cluster. Prior to hormonal intervention, we could
278 robustly assign the samples into all three clusters (Cl 1: n=23, Cl2: n=11, Cl3: n=8) with highly comparable
279 distributions as we previously reported in another cohort of patients (31) (**Supplementary Fig. S8A**). Our
280 pre- and post-treatment sampling now allowed us to investigate how individual tumors were affected by
281 neoadjuvant therapy. This revealed that three months of ENZ therapy pushed almost all of the tumors
282 towards our NE-like cluster 3 (**Fig. 4E; Supplementary Fig. S8B**). To assure that the observed effects are
283 not solely driven by the treatment-induced reduction in AR activity (**Fig. 4C and 4D**), we used a well-
284 established neuroendocrine PCa (NEPC) signature (34) to calculate gene expression fold changes pre- vs.
285 post-ENZ, which confirmed an induction of NE-like signaling upon treatment (**Fig. 4F**).
286 Collectively, these results demonstrate that three months of neoadjuvant ENZ therapy not only uniformly
287 diminishes AR signaling, but also pushes practically all of our primary PCa samples towards a NE-like gene
288 expression state independently of their original subtype.

289

290 **Post-treatment FOXA1 sites drive pro-survival gene programs, dictated by circadian clock** 291 **component ARNTL**

292 Having examined the global cistromic and transcriptomic changes upon ENZ therapy, we next
293 characterized the biological consequences of the observed FOXA1 reprogramming using integrative
294 analyses. We hypothesized that the newly acquired FOXA1 sites would be driving expression of genes
295 associated with tumor cell survival programs. Using H3K27ac HiChIP data generated in LNCaP cells (35),
296 pre- and post-treatment FOXA1 sites were coupled to their corresponding gene promoters (**Supplementary**
297 **Table S5**). Subsequently, genome-wide CRISPR knockout screen data from Project Achilles (DepMap
298 20Q1 Public; VCaP) were used to identify those genes essential for prostate cancer cell proliferation

299 (36,37). While genes associated with pre-treatment FOXA1 sites were not enriched for essentiality as
300 compared to all other CRISPR-targeted genes in the library, genes under control of post-treatment FOXA1
301 sites showed a significant enrichment ($P = 7.54 \times 10^{-12}$, Welch's t-test) for critical drivers of tumor cell
302 proliferation (**Fig. 5A**).

303 Based on our STARR-seq and RNA-seq data, we concluded that AR is likely not driving enhancer activity
304 at post-treatment FOXA1 sites (**Fig. 3F**; **Fig. 4C and 4D**). Therefore, we sought to identify transcription
305 factors involved in the activation of these regulatory regions that are selectively occupied by FOXA1
306 following treatment. To this end, we overlaid the genomic coordinates of the post-treatment enriched
307 FOXA1 binding sites with those identified in publicly available ChIP-seq datasets ($n = 13,976$) as part of the
308 Cistrome DB transcription factor ChIP-seq sample collection (38,39). Besides FOXA1 and AR, which were
309 expected to bind at these regions (**Fig. 3D**), we also identified the glucocorticoid receptor (encoded by the
310 *NR3C1* gene), which has previously been described to be upregulated upon antiandrogen treatment and
311 able to drive the expression of a subset of AR-responsive genes, conferring resistance to AR blockade (40-
312 42). Unexpectedly, the second most enriched transcription factor after FOXA1 was circadian rhythm core
313 component ARNTL (Aryl Hydrocarbon Receptor Nuclear Translocator Like; also known as BMAL1) which
314 has not previously been implicated in PCa biology (**Fig. 5B**). Interestingly, ARNTL transcript levels were
315 upregulated upon ENZ treatment ($P = 6.4 \times 10^{-3}$, Mann-Whitney U-test; **Fig. 5C**), which was accompanied
316 by increased H3K27ac ChIP-seq signals at the *ARNTL* locus (**Supplementary Fig. S9A**). Consistent with
317 this, tissue microarray IHC analysis also revealed elevated ARNTL protein levels after treatment when
318 comparing the prostatectomy specimens post-ENZ with those of matched untreated control patients ($P =$
319 6.89×10^{-19} , Fisher's exact test; **Fig. 5D**). To assess whether ARNTL levels are also associated with patient
320 outcome, we compared the average ARNTL gene expression of patients that did not experience a BCR
321 (responders, $n = 29$) with those that experienced an early BCR within ≤ 6 months post-surgery (non-
322 responders, $n = 8$; **Supplementary Table S1**). While pre-treatment ARNTL levels were not significantly
323 different between ENZ responders and non-responders, high ARNTL levels after treatment were associated
324 with poor clinical outcome ($P = 4.79 \times 10^{-3}$, Mann-Whitney U-test; **Fig. 5E**). Notably, the CLOCK protein,
325 which forms a heterodimer with ARNTL to activate transcription of core clock genes, didn't show differential
326 expression upon ENZ treatment (**Supplementary Fig. S9B**) and is also not associated with clinical

327 outcome (**Supplementary Fig. S9C**), hinting towards a treatment-induced role of ARNTL that is
328 independent of its canonical function in the circadian machinery.

329 Taken together, these data suggest that the circadian clock regulator ARNTL may be functionally involved
330 in ENZ resistance by driving tumor cell proliferation processes.

331

332 **Acquired ARNTL dependency in ENZ-resistant PCa cells**

333 To further investigate the relevance of ARNTL as a transcriptional driver at post-treatment FOXA1 sites,
334 we performed *in vitro* validation experiments. To this end, we used hormone-sensitive LNCaP PCa cells,
335 which we either cultured in full medium alone (Pre^{LNCaP}) or with ENZ for 48 hours (Post^{LNCaP}), mimicking our
336 clinical trial setting (**Fig. 6A**). Based on the acquisition of NE-like gene expression profiles post-ENZ (**Fig.**
337 **4E and 4F**), we also included the ENZ-resistant LNCaP-42D model (43) that possesses NE-features
338 (Res^{LNCaP-42D}; **Fig. 6A**), allowing us to further validate our patient-derived findings in cell lines recapitulating
339 the transcriptional features of post-treatment clinical specimens.

340 We performed FOXA1 ChIP-seq experiments in all three cell line conditions (**Supplementary Fig. S10A-**
341 **S10D; Supplementary Table S6**), which revealed highly similar FOXA1 chromatin binding dynamics as
342 observed in our clinical samples: While the pre-enriched FOXA1 sites identified *in vivo* showed less binding
343 upon treatment, we observed that merely 48 h of ENZ exposure was sufficient to strongly induce binding
344 at post-enriched sites, which was further increased in the long-term exposed, treatment-resistant LNCaP-
345 42D cell line (**Fig. 6B; Supplementary Fig. S10E**). Similarly, genome-wide correlation analyses indicated
346 that short-term ENZ treatment in cell lines induced FOXA1 reprogramming to regions that are FOXA1-
347 bound in treatment-resistant but not in treatment-naïve cells (**Supplementary Fig. S10F and S10G**).

348 Having shown that differential FOXA1 chromatin binding in tumors could be recapitulated *in vitro*, we next
349 sought to further assess the role of ARNTL in these pre-clinical models. Therefore, we first confirmed that
350 treatment with ENZ increased ARNTL protein levels in LNCaP and LNCaP-42D models (**Fig. 6C**),
351 recapitulating the clinical observations (**Fig. 5C and 5D**). Since cistromic ARNTL profiling has to date not
352 been reported in PCa models, we generated ARNTL ChIP-seq data (**Supplementary Fig. S11A-S11D**) to
353 validate its binding at post-treatment FOXA1 sites. Interestingly, while we already observed ARNTL binding
354 to these regulatory regions in the pre-treatment setting, this was strongly enhanced upon ENZ exposure

355 **(Fig. 6D; Supplementary Fig. S11E)**. To identify functional differences in ARNTL cistromes induced upon
356 treatment, we overlapped the ARNTL peaks identified in all tested cell line conditions, which revealed a
357 massive cistromic reprogramming upon ENZ treatment **(Fig. 6E; Supplementary Fig. S11F and S11G)**.
358 Notably, ~70% of ENZ-gained ARNTL peaks (n=1,752) in LNCaP cells were captured by the ARNTL
359 cistrome in treatment-resistant cells. Subsequent pathway over-representation analyses of genes coupled
360 to these Post^{LNCaP}-Res^{LNCaP-42D}-shared ARNTL binding sites revealed a treatment-induced enrichment for
361 gene sets implicated in cell cycle progression and cell division, further supporting a possible functional
362 involvement of ARNTL in sustaining tumor cell proliferation when AR is blocked by ENZ **(Fig. 6E)**. To
363 challenge this hypothesis, we assessed whether ARNTL-knockdown affects the viability of hormone-
364 sensitive and in particular of long-term ENZ-exposed cell lines. While ARNTL-targeting had minimal effect
365 on LNCaP cell proliferation (with or without ENZ), ARNTL knockdown significantly suppressed cell growth
366 of ENZ-resistant LNCaP-42D cells in the absence ($P = 0.031$, two-way ANOVA) and even more so in the
367 presence of ENZ ($P = 7 \times 10^{-4}$, two-way ANOVA), indicating that targeting ARNTL also partially restores
368 ENZ-sensitivity in this treatment-resistant cell line model **(Fig. 6F)**.

369 Overall, these data confirm the ENZ-induced FOXA1 reprogramming as observed in PCa patients upon
370 neoadjuvant antiandrogen therapy, and revealed an acquired dependency on circadian rhythm regulator
371 ARNTL to drive tumor cell growth – positioning ARNTL as a highly promising new drug target in combination
372 with ENZ for the treatment of high-risk PCa.

373

374 **Discussion**

375 In medicine, the evolutionary selection pressure as imposed by drug treatment has been a well-known
376 clinical challenge, ever since the first antibiotics were discovered in the early 20th century. Also in oncology,
377 clear escape mechanisms for both targeted therapeutics and systemic treatments are known for many
378 years, involving *ESR1* mutations in metastatic breast cancer (44), *EGFR* mutations in lung cancer (45),
379 *KRAS* mutations in metastatic colorectal cancer (46), but also somatic amplification of the *AR* locus and/or
380 an upstream *AR* enhancer in castration-resistant PCa (47,48). Apart from genetic alterations, also
381 epigenetic rewiring (7,41) or transdifferentiation are reported as mechanisms of resistance, including

382 treatment-emergent neuroendocrine (NE) prostate cancers that occur as an adaptive response under the
383 pressure of prolonged AR-targeted therapy (49,50).

384 Our unique clinical trial design with paired pre- and post-treatment biopsies of high-risk primary PCa treated
385 with ENZ monotherapy, allowed us to unravel global ENZ-induced alterations in gene regulation. We report
386 that large-scale treatment-induced dedifferentiation in PCa may be a gradual process, of which the early
387 signs are identified on transcriptomic level within the first months of treatment onset. While complete
388 adenocarcinoma-NE transdifferentiation was not observed in any of our samples, cellular plasticity
389 characterized by transcriptomic features of NE disease may not only be present prior to treatment (31), but
390 also become enriched upon short-term endocrine treatment exposure.

391 In PCa development (5,51) and progression (7), AR has been reported to expose substantial plasticity in
392 its enhancer repertoire, and we now illustrate this is also the case in primary disease upon short-term
393 treatment. Besides AR, FOXA1 is considered a master transcription factor and critical prostate lineage
394 specific regulator acting in PCa, that upon overexpression during tumorigenesis gives rise to a tumor-
395 specific AR cistrome. Also in NEPC, FOXA1 cistromes are reprogrammed (52), which indicates a direct
396 AR-independent role of FOXA1 in PCa progression. Our study confirms these observations and shows that,
397 while co-occupied by AR, the pre- and post-ENZ enriched FOXA1 sites appeared indifferent to AR
398 signaling.

399 The functional implications of the pre-treatment FOXA1 sites remain unclear, as those regions were
400 inactive, both in primary tissues as well as in reporter assays. A subset of these *cis*-regulatory elements
401 demarcates developmental epigenomic programs, that we previously reported as being occupied by
402 FOXA1 from prostate development to tumorigenesis and metastatic progression (7), whereas others may
403 be relevant for different physiological processes.

404 The treatment-induced cistromic repositioning of FOXA1 initiated a thus far unknown transcriptional
405 rewiring, in which ARNTL, a classical circadian rhythm regulator and dimerization partner of CLOCK,
406 compensates for AR inhibition and becomes essential to rescue cellular proliferation signals. Recently, it
407 has been reported that CRY1 – a transcriptional coregulator of ARNTL – is AR-regulated in PCa, and
408 modulates DNA repair processes in a circadian manner (53). The current data illustrate that circadian
409 rhythm may have a potential impact on drug response, as most clock components are regulated on

410 transcriptional level, in time. Our data now show that AR blockade forces tumor cells to adapt epigenetically,
411 upon which these cells – over time – become dependent on ARNTL as a transcriptional regulator of
412 proliferation processes. This acquired cellular vulnerability appears to be dependent on whether or not AR
413 activity is inhibited and cells have had time to achieve full epigenetic reprogramming, explaining the limited
414 effect of ARNTL knockdown in hormone-sensitive PCa cells, as compared to the long-term ENZ-exposed
415 treatment-resistant model.

416 With the identification of ARNTL as a rescue mechanism for tumor cells to evade AR blockade, the next
417 question presents whether ARNTL could serve as a novel therapeutic target, which should be further
418 pursued in future drug development and clinical research. Being critically relevant for circadian rhythm
419 regulation, it would be imperative to balance ARNTL targeting in relation to any adverse side-effects.
420 Additionally, we demonstrate that the surprisingly dynamic enhancer repertoire of FOXA1 is not only critical
421 in prostate tumorigenesis (5) and neuroendocrine differentiation (52), but also appears crucial in evading
422 AR therapy-induced growth inhibition, further supporting the rationale to intensify efforts in targeting this
423 highly tissue-selective, yet critical transcriptional regulator, directly or indirectly (54).

424

425 **Methods**

426 **Study design**

427 Primary PCa tissues before and after enzalutamide (ENZ) treatment were acquired as part of the phase
428 2, prospective, single-arm DARANA study (ClinicalTrials.gov #NCT03297385) at the Netherlands Cancer
429 Institute Antoni van Leeuwenhoek hospital. To allow sample size calculation, we performed a survey into
430 the surgical margins of 1492 in-house prostatectomy specimens (Gleason ≥ 7), not treated with
431 antihormonal therapy prior to surgery, which revealed 34% not-radical resections. Earlier randomized
432 studies on neoadjuvant androgen ablation showed reductions in positive surgical margin rate of at least
433 50% (55-57). To detect a reduction of positive surgical margins from 34% to 17% with a power of 80% and
434 an alpha set at 0.05, 55 patients needed to be included. Inclusion criteria were over 18 years of age,
435 Gleason ≥ 7 PCa and planned for prostatectomy. Prior to treatment a multi-parametric MRI scan was made
436 to identify tumors in the prostate (cT-stage) and pelvic lymph node metastasis (cN-stage). Patients were
437 treated with ENZ, once daily 160 mg P.O. without androgen deprivation therapy, for three months prior to

438 RALP and a pelvic lymph node dissection. 55 patients completed therapy without dose adjustments, while
439 one patient (DAR37) discontinued ENZ three weeks prematurely. The resection specimen was assessed
440 for prostate tumor stage (ypT-stage) and the pelvic lymph nodes (ypN-stage). Primary clinical outcome
441 measure was positive margins rate and secondary endpoints were differences in pre- and post-treatment
442 T (tumor) and N (lymph node) stage and median time to biochemical recurrence, defined as two consecutive
443 rises of serum PSA with a minimal level of ≥ 0.2 ng/mL. The trial was approved by the institutional review
444 board of the Netherlands Cancer Institute, informed consent was signed by all participants enrolled in the
445 study, and all research was carried out in accordance with relevant guidelines and regulations.

446

447 **Pre- and post-treatment sampling**

448 Prior to ENZ intervention, 4 pre-operative MRI-guided 18-gauche core needle tumor biopsies were taken
449 per patient. Directly after prostatectomy, 8 additional tumor-targeted core needle biopsies (4x 14 gauche,
450 4x 5 mm) were taken from prostatectomy specimens *ex vivo*, using previous MRI information and palpation.
451 Biopsy and prostatectomy specimens were fresh frozen (FF) or formalin-fixed paraffin-embedded (FFPE)
452 for ChIP-seq and CNV-seq, or RNA-seq and immunohistochemistry analyses, respectively. Prior to ChIP-
453 seq experiments, FF material was cut in 30 μ m sections, while FFPE material was cut in 10 μ m sections
454 prior to RNA extraction. Tissue sections were examined pathologically for tumor cell content and only
455 samples with a tumor cell percentage of $\geq 50\%$ were used for further downstream analyses.

456

457 **ChIP-seq**

458 Chromatin immunoprecipitations on PCa tissue specimens and cell line models were performed as
459 previously described (58). In brief, cryosectioned tissue samples were double-crosslinked in solution A
460 (50 mM HEPES-KOH, 100 mM NaCl, 1 mM EDTA, 0.5 mM EGTA), first supplemented with 2 mM
461 disuccinimidyl glutarate (DSG; CovaChem) for 25 min at room temperature. Then, 1% formaldehyde
462 (Merck) was added for 20 min and subsequently quenched with a surplus of 2.5 M glycine. Cell lines were
463 crosslinked using single-agent fixation. Therefore, 1% formaldehyde was added to the cell culture medium
464 and incubated at room temperature for 10 min, followed by glycine-quenching as described above. Tissue
465 and cell line samples were lysed as described (59) and sonicated for at least 10 cycles (30 sec on; 30 sec

466 off) using a PicoBioruptor (Diagenode). For each ChIP, 5 μ g of antibody were conjugated to 50 μ L magnetic
467 protein A or G beads (10008D or 10009D, Thermo Fisher Scientific). The following antibodies were used:
468 AR (06-680, Merck Millipore), FOXA1 (ab5089, Abcam), H3K27ac (39133, Active Motif), and ARNTL
469 (ab93806, Abcam).

470 Immunoprecipitated DNA was processed for library preparation using a KAPA library preparation kit
471 (KK8234, Roche) and generated libraries were sequenced on the Illumina HiSeq2500 platform using the
472 single end protocol with a read length of 65-bp, and aligned to the human reference genome hg19 using
473 Burrows-Wheeler Aligner (v0.5.10) (60). Reads were filtered based on mapping quality (MAPQ \geq 20) and
474 duplicate reads were removed. Peak calling over input controls (per tissue sample or cell line) was
475 performed using MACS2 (v2.1.1) and Dfilter (v1.6) for tissues, and MACS2 (v2.1.2) for cell lines (61,62).
476 For tissue samples, only the peaks shared by both peak callers were used for downstream analyses.
477 DeepTools (v2.5.3) was used to calculate read counts in peaks (FRiP) (63). Read counts and the number
478 of aligned reads, as well as normalized strand coefficient (NSC) and relative strand correlation (RSC), which
479 were calculated using phantompeaktools (v1.10.1) (64), are shown in **Supplementary Table S2** for tissue
480 ChIP-seq data and **Supplementary Table S6** for cell line ChIP-seq data. Tissue ChIP-seq samples that
481 passed the following quality control measures were included in the final analyses; tumor cell percentage \geq
482 50%, ChIP-qPCR enrichment, and more than 100 peaks called (**Supplementary Fig. S1B**).

483 For visualization of cell line ChIP-seq data, an average enrichment signal was generated by merging
484 mapped reads of replicate samples using SAMtools (v1.10-3) (65).

485 Genome browser snapshots, tornado and average density plots were generated using EaSeq (v1.101) (66).
486 Genomic distribution and motif enrichment analyses were performed using the CEAS and the SeqPos motif
487 tools on Galaxy Cistrome (67), respectively. Cistrome Toolkit was used to probe which TFs and chromatin
488 regulators have a significant binding overlap with the differential FOXA1 peak sets (39). For this, genomic
489 coordinates of high-confidence binding sites (FC \geq 1.2) were converted between assemblies (from hg19 to
490 hg38), using the UCSC genome browser liftOver tool (68). The DiffBind R package (v2.10) was used to
491 generate correlation heatmaps and PCA plots based on occupancy, to perform differential binding analyses
492 using a false discovery rate (FDR) $<$ 0.05, and to generate consensus peaklists (69).

493 ChIP-seq signal of various datasets (FOXA1, AR and H3K27ac from this study; AR, H3K27ac and
494 H3K27me3 from a previously reported study (31)) at differential and consensus FOXA1 sites was
495 investigated by counting mapped reads in FOXA1 peak regions using bedtools multicov (v2.27.1) (70).
496 Readcounts were subsequently z-transformed and visualized using the aheatmap function from the R
497 package NMF (v0.21.0) (71) with a color scheme from RColorBrewer (v1.1-2; [https://CRAN.R-](https://CRAN.R-project.org/package=RColorBrewer)
498 [project.org/package=RColorBrewer](https://CRAN.R-project.org/package=RColorBrewer)). To determine significance in binding site occupancy differences
499 between pre- and post-treatment FOXA1 sites, median z-transformed readcounts were calculated per
500 sample and compared using a Mann-Whitney U-test. These median readcounts per sample were also used
501 to assess the correlation between ChIP-seq signals of AR, FOXA1 and H3K27ac at pre-enriched, post-
502 enriched and consensus FOXA1 binding sites.

503 Bedtools intersect (v2.27.1) (70) was used to determine overlap of differential FOXA1 binding sites and
504 inactive, constitutively active and inducible AR-binding sites.

505 To assign FOXA1 and ARNTL binding regions to potential target genes, we overlapped differential FOXA1
506 binding sites with H3K27ac HiChIP data (35) using bedtools intersect. To assess whether or not genes
507 coupled to FOXA1 binding sites were considered to be essential for the VCAP prostate cancer cell line, we
508 used the DepMap (Broad 2020) 20Q1 Public gene effect dataset (36). Gene set overlaps between genes
509 linked to ChIP-seq binding sites and the Molecular Signatures Database (v7.4) were computed using Gene
510 Set Enrichment Analysis (GSEA) (72) with an FDR q-value cutoff ≤ 0.05 .

511

512 **RNA-seq**

513 Prior to RNA isolation, FFPE material was pathologically assessed. The expert pathologist scored tumor
514 cell percentage and indicated most tumor-dense regions for isolation on a hematoxylin and eosin (H&E)
515 slide. RNA and DNA from FFPE material were simultaneously isolated from 3-10 sections (depending on
516 tumor size) of 10 μm using the AllPrep DNA/RNA FFPE isolation kit (80234, Qiagen) and the QIAcube
517 according to the manufacturer's instructions. cDNA was synthesized from 250 ng RNA using SuperScript
518 III Reverse Transcriptase (Invitrogen) with random hexamer primers.

519 For RNA-seq, strand-specific libraries were generated with the TruSeq RNA Exome kit (Illumina) and
520 sequenced on the Illumina HiSeq2500 platform using the single end protocol with a read length of 65-bp.

521 Sequencing data was aligned to the human reference genome hg38 using TopHat (v2.1.0 using bowtie
522 1.1.0) (73) and the number of reads per gene was measured with HTSeq count (v0.5.3) (74).

523 For QC purposes, total readcounts per sample were determined and hierarchical clustering based on the
524 Euclidean distance was applied. Samples with a readcount ≥ 2 standard deviations below the mean of all
525 sample readcounts were removed, as well as samples that clustered in a separate branch.

526 Global gene expression differences between pre- and post-treatment samples passing QC were
527 determined using DESeq2 (v1.22.2) (75). Significance of expression level differences between pre- and
528 post-treatment samples was determined using a paired t-test.

529 Gene set enrichment was performed using pre-ranked GSEA (72) based on the Wald statistic provided by
530 DESeq2. For visualization purposes, the data were Z-transformed per gene. Heatmaps of gene expression
531 values were created using the aheatmap function from the R package NMF (v0.21.0) (71) with a color
532 scheme from RColorBrewer (v1.1-2; <https://CRAN.R-project.org/package=RColorBrewer>).

533 To assign samples to previously described PCa subtypes (31), the z-transformed expression levels of the
534 top ~100 most differentially expressed genes (n=285) in each of the three clusters were investigated. Using
535 these values, samples were clustered based on their Pearson correlation. The resulting tree was divided
536 into 3 clusters, corresponding to the previously published PCa subtypes. Potential transitioning of samples
537 from one cluster to another after treatment was visualized using a riverplot (v0.6; [https://CRAN.R-](https://CRAN.R-project.org/package=riverplot)
538 [project.org/package=riverplot](https://CRAN.R-project.org/package=riverplot)).

539 To calculate fold changes of neuroendocrine scores upon treatment, expression of 70 neuroendocrine
540 signature genes were obtained from castration-resistant neuroendocrine and prostate adenocarcinoma
541 samples as published previously (34). The expression of 5 of the 70 neuroendocrine signature genes were
542 not included in the analysis (KIAA0408, SOGA3, LRRC16B, ST8SIA3, SVOP) because the genes are not
543 expressed in these samples. Expression fold changes between paired pre- and post-treatment samples
544 were calculated (n=39) and concordance in gene expression differences (fold change sign) were measured
545 using Pearson correlation.

546

547 **CNV-seq**

548 Low-coverage whole-genome samples (ChIP-seq inputs), sequenced single-end 65-bp on a HiSeq 2500
549 system were aligned to hg19 with Burrows-Wheeler Aligner backtrack algorithm (v0.5.10) (60). The
550 mappability per 20-kb on the genome, for a samples' reads, phred quality 37 and higher, was rated against
551 a similarly obtained mappability for all known and tiled 65-bp subsections of hg19. Sample counts were
552 corrected per bin for local GC effects using a non-linear loess fit of mappabilities over 0.8 on autosomes.
553 Reference values were scaled according to the slope of a linear fit, forced to intercept at the origin, of
554 reference mappabilities after GC correction. Ratios of corrected sample counts and reference values left
555 out bins with mappability below 0.2 or overlapping ENCODE blacklisted regions (76).
556 Copy number log ratios were smoothed and segmented using the R package DNACopy (v1.50.1;
557 <https://bioconductor.org/packages/release/bioc/html/DNACopy.html>) with the parameters set to
558 $\alpha=0.0000000001$, $\text{undo.SD}=2$, and $\text{undo.splits}=\text{"sdundo"}$. Bedtools intersect (v2.27.1) (70) was used
559 to determine overlap between copy number segments and differential FOXA1 binding sites. These data
560 were subsequently visualized using the aheatmap function from the R package NMF (v0.21.0) (71) with a
561 color scheme from RColorBrewer (v1.1-2; <https://CRAN.R-project.org/package=RColorBrewer>).
562 To correlate FOXA1 ChIP-seq signal with copy number status at differential FOXA1 sites, we employed the
563 z-transformed FOXA1 ChIP-seq readcounts as described in the ChIP-seq section. The difference in
564 transformed ChIP-seq readcounts and the difference in normalized segmented copy number data between
565 matched post-treatment and pre-treatment samples was calculated for every patient. Subsequently, the
566 Pearson correlation between these two sets of differences was calculated.

567 **Immunohistochemistry**

568 For immunohistochemistry (IHC) analysis, we matched our ENZ-treated patient cohort (n=51) in a 1:2
569 ratio to untreated control patients (not receiving ENZ prior to prostatectomy; n=110) based on
570 clinicopathological parameters (initial PSA, Gleason score, TNM stage, age) using the R package MatchIt
571 (v.4.1.0) (77).

572 Tissue microarrays (TMAs) were prepared containing 3 cores per FFPE tumor sample. Tumor-dense areas
573 in FFPE megablocks were marked by an expert pathologist on a H&E slide. Cores were drilled in a receptor
574 block using the TMA grandmaster (3D Histech/Sysmex). Next, cores were taken from the donor block and

575 placed in the receptor block using the manual tissue arrayer (4508-DM, Beecher instruments). The filled
576 receptor block was placed in a 70°C stove for 9 minutes and cooled overnight at RT.

577 Immunohistochemistry was applied to TMA slides using a BenchMark Ultra autostainer (Ventana Medical
578 Systems). In brief, paraffin sections were cut at 3 µm, heated at 75°C for 28 minutes and deparaffinized in
579 the instrument with EZ prep solution (Ventana Medical Systems). Heat-induced antigen retrieval was
580 carried out using Cell Conditioning 1 (CC1, Ventana Medical Systems) for 64 minutes at 95°C.

581 For ARNTL IHC, TMAs were stained with an anti-ARNTL antibody (ab230822, Abcam) for 60 minutes at
582 36°C using a 1:1000 antibody dilution. Bound antibody was detected using the OptiView DAB Detection Kit
583 (Ventana Medical Systems). Slides were counterstained with hematoxylin and bluing reagent (Ventana
584 Medical Systems).

585 ARNTL staining intensity (weak, moderate, strong) in tumor cells was scored by an expert pathologist.
586 Tissues scored for at least two cores were analyzed and used for statistical analysis.

587

588 **Cell lines and cell culture**

589 LNCaP human PCa cell line was purchased from the American Type Culture Collection (ATCC).
590 Enzalutamide-resistant LNCaP-42D cells were described previously (43). LNCaP cells were maintained in
591 RPMI-1640 medium (Gibco, Thermo Fisher Scientific) supplemented with 10% FBS (Sigma-Aldrich).
592 LNCaP-42D cells were maintained in RPMI-1640 medium containing 10% FBS and 10 µM ENZ. Cell lines
593 were subjected to regular mycoplasma testing and all cell lines underwent authentication by short tandem
594 repeat profiling (Eurofins Genomics). For hormone stimulation with synthetic androgen, cells were treated
595 with 10 nM R1881 (PerkinElmer) for 48 h. For *in vitro* AR blockade, cells were treated with 10 µM ENZ
596 (MedChemExpress) and harvested at the indicated time points.

597

598 **Transient cell line transfections**

599 Transient transfections of cell lines were performed according to the manufacturer's instructions using
600 Lipofectamine 2000 (Invitrogen) or Lipofectamine RNAiMAX (Invitrogen) for overexpression or siRNA
601 knockdown experiments, respectively. ARNTL containing expression plasmid was obtained from the

602 CCSB-Broad Lentiviral Expression Library. siRNA oligos targeting ARNTL (M-010261-00-0005), and the
603 non-targeting control (D-001206-14) were purchased from Dharmacon.

604

605 **Western blotting**

606 Total proteins were extracted from cells using Laemmli lysis buffer, supplemented with a complete
607 protease inhibitor cocktail (Roche). Per sample, 40 μ g of protein was resolved by SDS-PAGE (10%) and
608 transferred on nitrocellulose membranes (Santa Cruz Biotechnology). The following antibodies were used
609 for Western blot stainings: ARNTL (ab93806, Abcam), PSA (5365, Cell Signaling Technology), and ACTIN
610 (MAB1501R, Merck Millipore). Blots were incubated overnight at 4°C with designated primary antibodies at
611 1:1000 (ARNTL, PSA) or 1:5000 (ACTIN) dilution, and visualized using the Odyssey system (Li-Cor
612 Biosciences).

613

614 **Cell viability assay**

615 For cell viability assays, LNCaP or LNCaP-42D cells were seeded at 2×10^3 cells per well in 96-well
616 plates (Greiner) \pm 10 μ M ENZ, and reverse transfected with 50 nM siRNA (Dharmacon) using Lipofectamine
617 RNAiMAX (Invitrogen). Cell viability was assessed 7 days post-transfection using the CellTiter-Glo
618 Luminescent Cell Viability Assay kit (Promega), as per the manufacturer's instructions.

619

620 **Statistical analysis**

621 For differential binding and differential gene expression analyses (pre- vs. post-ENZ), an FDR cutoff $<$
622 0.05 ($P < 0.01$) and $P_{adj} < 0.01$ was used, respectively. A Mann-Whitney U-test was used to determine
623 differences in region readcounts (adjusted for multiple testing using FDR) and differences in gene
624 expression levels before and after ENZ treatment. For peak set and gene set overlaps, Fisher's exact or
625 Welch Two Sample t-tests were applied. A Fisher's exact test was used to determine differences in IHC
626 staining intensity. Differences in cell viability were tested using a two-way ANOVA followed by Tukey's
627 multiple comparisons test (GraphPad Prism 9). Corresponding bar chart shows the mean with error bars
628 representing the SD of three independent experiments. All boxplots indicate the median (center line), upper-
629 (75) and lower - (25) quartile range (box limits) and 1.5 x interquartile range (whiskers). Significance is

630 indicated as follows: ns, $P > 0.05$; *, $P < 0.05$; **, $P < 0.01$; ***, $P < 0.001$; ****, $P < 0.0001$. Further details
631 of statistical tests are provided in the figure legends.

632

633 **Declaration of Potential Conflicts of Interest**

634 W. Zwart, A.M. Bergman and H. van der Poel received research funding from Astellas Pharma B.V.
635 (Leiden, the Netherlands). No potential conflicts of interest were disclosed by the other authors.

636

637 **Acknowledgements**

638 The authors would like to thank the NKI-AVL Core Facility Molecular Pathology & Biobanking (CFMPB)
639 for technical assistance, the NKI Genomics Core Facility (GCF) for next generation sequencing and
640 bioinformatics support, and the NKI Research High Performance Computing facility (RHPC) for
641 computational infrastructure. We also thank all Zwart/Bergman lab members for fruitful discussions and
642 technical advice. Finally, we would like to thank all patients and clinical staff who were involved in the
643 DARANA trial.

644

645 **Grant Support**

646 This work was supported by Movember (NKI01 to A.M. Bergman and W. Zwart), KWF Dutch Cancer
647 Society (10084 ALPE to A.M. Bergman and W. Zwart), KWF Dutch Cancer Society/Alpe d'HuZes Bas
648 Mulder Award (NKI 2014-6711 to W. Zwart), Netherlands Organization for Scientific Research (NWO-VIDI-
649 016.156.401 to W. Zwart), and Astellas Pharma (to W. Zwart, A.M. Bergman, H. van der Poel).

650

651 **References**

- 652 1. Huggins C, Hodges CV. Studies on prostatic cancer. I. The effect of castration, of estrogen and
653 androgen injection on serum phosphatases in metastatic carcinoma of the prostate. *CA Cancer J*
654 *Clin* **1972**;22(4):232-40 doi 10.3322/canjclin.22.4.232.
- 655 2. Zhang Z, Chng KR, Lingadahalli S, Chen Z, Liu MH, Do HH, *et al.* An AR-ERG transcriptional
656 signature defined by long-range chromatin interactomes in prostate cancer cells. *Genome Res*
657 **2019**;29(2):223-35 doi 10.1101/gr.230243.117.
- 658 3. Stelloo S, Bergman AM, Zwart W. Androgen receptor enhancer usage and the chromatin regulatory
659 landscape in human prostate cancers. *Endocr Relat Cancer* **2019**;26(5):R267-R85 doi
660 10.1530/ERC-19-0032.

- 661 4. Stelloo S, Nevedomskaya E, Kim Y, Hoekman L, Bleijerveld OB, Mirza T, *et al.* Endogenous
662 androgen receptor proteomic profiling reveals genomic subcomplex involved in prostate
663 tumorigenesis. *Oncogene* **2018**;37(3):313-22 doi 10.1038/onc.2017.330.
- 664 5. Pomerantz MM, Li F, Takeda DY, Lenci R, Chonkar A, Chabot M, *et al.* The androgen receptor
665 cistrome is extensively reprogrammed in human prostate tumorigenesis. *Nat Genet*
666 **2015**;47(11):1346-51 doi 10.1038/ng.3419.
- 667 6. Gerhardt J, Montani M, Wild P, Beer M, Huber F, Hermanns T, *et al.* FOXA1 promotes tumor
668 progression in prostate cancer and represents a novel hallmark of castration-resistant prostate
669 cancer. *Am J Pathol* **2012**;180(2):848-61 doi 10.1016/j.ajpath.2011.10.021.
- 670 7. Pomerantz MM, Qiu X, Zhu Y, Takeda DY, Pan W, Baca SC, *et al.* Prostate cancer reactivates
671 developmental epigenomic programs during metastatic progression. *Nat Genet* **2020**;52(8):790-9
672 doi 10.1038/s41588-020-0664-8.
- 673 8. Cirillo LA, Lin FR, Cuesta I, Friedman D, Jarnik M, Zaret KS. Opening of compacted chromatin by
674 early developmental transcription factors HNF3 (FoxA) and GATA-4. *Mol Cell* **2002**;9(2):279-89 doi
675 10.1016/s1097-2765(02)00459-8.
- 676 9. Lupien M, Eeckhoute J, Meyer CA, Wang Q, Zhang Y, Li W, *et al.* FoxA1 translates epigenetic
677 signatures into enhancer-driven lineage-specific transcription. *Cell* **2008**;132(6):958-70 doi
678 10.1016/j.cell.2008.01.018.
- 679 10. Sahu B, Laakso M, Ovaska K, Mirtti T, Lundin J, Rannikko A, *et al.* Dual role of FoxA1 in androgen
680 receptor binding to chromatin, androgen signalling and prostate cancer. *EMBO J*
681 **2011**;30(19):3962-76 doi 10.1038/emboj.2011.328.
- 682 11. Teng M, Zhou S, Cai C, Lupien M, He HH. Pioneer of prostate cancer: past, present and the future
683 of FOXA1. *Protein Cell* **2021**;12(1):29-38 doi 10.1007/s13238-020-00786-8.
- 684 12. Grasso CS, Wu YM, Robinson DR, Cao X, Dhanasekaran SM, Khan AP, *et al.* The mutational
685 landscape of lethal castration-resistant prostate cancer. *Nature* **2012**;487(7406):239-43 doi
686 10.1038/nature11125.
- 687 13. Barbieri CE, Baca SC, Lawrence MS, Demichelis F, Blattner M, Theurillat JP, *et al.* Exome
688 sequencing identifies recurrent SPOP, FOXA1 and MED12 mutations in prostate cancer. *Nat Genet*
689 **2012**;44(6):685-9 doi 10.1038/ng.2279.
- 690 14. Cancer Genome Atlas Research N. The Molecular Taxonomy of Primary Prostate Cancer. *Cell*
691 **2015**;163(4):1011-25 doi 10.1016/j.cell.2015.10.025.
- 692 15. Robinson D, Van Allen EM, Wu YM, Schultz N, Lonigro RJ, Mosquera JM, *et al.* Integrative Clinical
693 Genomics of Advanced Prostate Cancer. *Cell* **2015**;162(2):454 doi 10.1016/j.cell.2015.06.053.
- 694 16. Wedge DC, Gudem G, Mitchell T, Woodcock DJ, Martincorena I, Ghori M, *et al.* Sequencing of
695 prostate cancers identifies new cancer genes, routes of progression and drug targets. *Nat Genet*
696 **2018**;50(5):682-92 doi 10.1038/s41588-018-0086-z.
- 697 17. Adams EJ, Karthaus WR, Hoover E, Liu D, Gruet A, Zhang Z, *et al.* FOXA1 mutations alter
698 pioneering activity, differentiation and prostate cancer phenotypes. *Nature* **2019**;571(7765):408-12
699 doi 10.1038/s41586-019-1318-9.
- 700 18. Parolia A, Cieslik M, Chu SC, Xiao L, Ouchi T, Zhang Y, *et al.* Distinct structural classes of activating
701 FOXA1 alterations in advanced prostate cancer. *Nature* **2019**;571(7765):413-8 doi
702 10.1038/s41586-019-1347-4.
- 703 19. Mottet N, van den Bergh RCN, Briers E, Van den Broeck T, Cumberbatch MG, De Santis M, *et al.*
704 EAU-EANM-ESTRO-ESUR-SIOG Guidelines on Prostate Cancer-2020 Update. Part 1: Screening,
705 Diagnosis, and Local Treatment with Curative Intent. *Eur Urol* **2021**;79(2):243-62 doi
706 10.1016/j.eururo.2020.09.042.

- 707 20. Roehl KA, Han M, Ramos CG, Antenor JA, Catalona WJ. Cancer progression and survival rates
708 following anatomical radical retropubic prostatectomy in 3,478 consecutive patients: long-term
709 results. *J Urol* **2004**;172(3):910-4 doi 10.1097/01.ju.0000134888.22332.bb.
- 710 21. Harris WP, Mostaghel EA, Nelson PS, Montgomery B. Androgen deprivation therapy: progress in
711 understanding mechanisms of resistance and optimizing androgen depletion. *Nat Clin Pract Urol*
712 **2009**;6(2):76-85 doi 10.1038/ncpuro1296.
- 713 22. Cornford P, van den Bergh RCN, Briers E, Van den Broeck T, Cumberbatch MG, De Santis M, *et*
714 *al.* EAU-EANM-ESTRO-ESUR-SIOG Guidelines on Prostate Cancer. Part II-2020 Update:
715 Treatment of Relapsing and Metastatic Prostate Cancer. *Eur Urol* **2021**;79(2):263-82 doi
716 10.1016/j.eururo.2020.09.046.
- 717 23. Zong Y, Goldstein AS. Adaptation or selection--mechanisms of castration-resistant prostate
718 cancer. *Nat Rev Urol* **2013**;10(2):90-8 doi 10.1038/nrurol.2012.237.
- 719 24. Linder S, van der Poel HG, Bergman AM, Zwart W, Prekovic S. Enzalutamide therapy for advanced
720 prostate cancer: efficacy, resistance and beyond. *Endocr Relat Cancer* **2018**;26(1):R31-R52 doi
721 10.1530/ERC-18-0289.
- 722 25. Scher HI, Fizazi K, Saad F, Taplin ME, Sternberg CN, Miller K, *et al.* Increased survival with
723 enzalutamide in prostate cancer after chemotherapy. *N Engl J Med* **2012**;367(13):1187-97 doi
724 10.1056/NEJMoa1207506.
- 725 26. Beer TM, Armstrong AJ, Rathkopf DE, Loriot Y, Sternberg CN, Higano CS, *et al.* Enzalutamide in
726 metastatic prostate cancer before chemotherapy. *N Engl J Med* **2014**;371(5):424-33 doi
727 10.1056/NEJMoa1405095.
- 728 27. Armstrong AJ, Szmulewitz RZ, Petrylak DP, Holzbeierlein J, Villers A, Azad A, *et al.* ARCHES: A
729 Randomized, Phase III Study of Androgen Deprivation Therapy With Enzalutamide or Placebo in
730 Men With Metastatic Hormone-Sensitive Prostate Cancer. *J Clin Oncol* **2019**;37(32):2974-86 doi
731 10.1200/JCO.19.00799.
- 732 28. Hussain M, Fizazi K, Saad F, Rathenborg P, Shore N, Ferreira U, *et al.* Enzalutamide in Men with
733 Nonmetastatic, Castration-Resistant Prostate Cancer. *N Engl J Med* **2018**;378(26):2465-74 doi
734 10.1056/NEJMoa1800536.
- 735 29. Prekovic S, van den Broeck T, Linder S, van Royen ME, Houtsmuller AB, Handle F, *et al.* Molecular
736 underpinnings of enzalutamide resistance. *Endocr Relat Cancer* **2018**;25(11):R545-R57 doi
737 10.1530/ERC-17-0136.
- 738 30. Gao N, Zhang J, Rao MA, Case TC, Mirosevich J, Wang Y, *et al.* The role of hepatocyte nuclear
739 factor-3 alpha (Forkhead Box A1) and androgen receptor in transcriptional regulation of prostatic
740 genes. *Mol Endocrinol* **2003**;17(8):1484-507 doi 10.1210/me.2003-0020.
- 741 31. Stelloo S, Nevedomskaya E, Kim Y, Schuurman K, Valle-Encinas E, Lobo J, *et al.* Integrative
742 epigenetic taxonomy of primary prostate cancer. *Nat Commun* **2018**;9(1):4900 doi
743 10.1038/s41467-018-07270-2.
- 744 32. Kron KJ, Murison A, Zhou S, Huang V, Yamaguchi TN, Shiah YJ, *et al.* TMPRSS2-ERG fusion co-
745 opts master transcription factors and activates NOTCH signaling in primary prostate cancer. *Nat*
746 *Genet* **2017**;49(9):1336-45 doi 10.1038/ng.3930.
- 747 33. Huang C-CF, Lingadahalli S, Morova T, Ozturan D, Hu E, Lok Yu IP, *et al.* Functional mapping of
748 androgen receptor enhancer activity. *bioRxiv* **2020**:2020.08.18.255232 doi
749 10.1101/2020.08.18.255232.
- 750 34. Beltran H, Prandi D, Mosquera JM, Benelli M, Puca L, Cyrta J, *et al.* Divergent clonal evolution of
751 castration-resistant neuroendocrine prostate cancer. *Nat Med* **2016**;22(3):298-305 doi
752 10.1038/nm.4045.

- 753 35. Giambartolomei C, Seo J-H, Schwarz T, Freund MK, Johnson RD, Spisak S, *et al.* H3k27ac-HiChIP
754 in prostate cell lines identifies risk genes for prostate cancer susceptibility. *bioRxiv*
755 **2020**:2020.10.23.352351 doi 10.1101/2020.10.23.352351.
- 756 36. Meyers RM, Bryan JG, McFarland JM, Weir BA, Sizemore AE, Xu H, *et al.* Computational correction
757 of copy number effect improves specificity of CRISPR-Cas9 essentiality screens in cancer cells.
758 *Nat Genet* **2017**;49(12):1779-84 doi 10.1038/ng.3984.
- 759 37. Dempster JM, Rossen J, Kazachkova M, Pan J, Kugener G, Root DE, *et al.* Extracting Biological
760 Insights from the Project Achilles Genome-Scale CRISPR Screens in Cancer Cell Lines. *bioRxiv*
761 **2019**:720243 doi 10.1101/720243.
- 762 38. Layer RM, Pedersen BS, DiSera T, Marth GT, Gertz J, Quinlan AR. GIGGLE: a search engine for
763 large-scale integrated genome analysis. *Nat Methods* **2018**;15(2):123-6 doi 10.1038/nmeth.4556.
- 764 39. Zheng R, Wan C, Mei S, Qin Q, Wu Q, Sun H, *et al.* Cistrome Data Browser: expanded datasets
765 and new tools for gene regulatory analysis. *Nucleic Acids Res* **2019**;47(D1):D729-D35 doi
766 10.1093/nar/gky1094.
- 767 40. Arora VK, Schenkein E, Murali R, Subudhi SK, Wongvipat J, Balbas MD, *et al.* Glucocorticoid
768 receptor confers resistance to antiandrogens by bypassing androgen receptor blockade. *Cell*
769 **2013**;155(6):1309-22 doi 10.1016/j.cell.2013.11.012.
- 770 41. Shah N, Wang P, Wongvipat J, Karthaus WR, Abida W, Armenia J, *et al.* Regulation of the
771 glucocorticoid receptor via a BET-dependent enhancer drives antiandrogen resistance in prostate
772 cancer. *Elife* **2017**;6 doi 10.7554/eLife.27861.
- 773 42. Palit SA, Vis D, Stelloo S, Liefink C, Prekovic S, Bekers E, *et al.* TLE3 loss confers AR inhibitor
774 resistance by facilitating GR-mediated human prostate cancer cell growth. *Elife* **2019**;8 doi
775 10.7554/eLife.47430.
- 776 43. Bishop JL, Thaper D, Vahid S, Davies A, Ketola K, Kuruma H, *et al.* The Master Neural
777 Transcription Factor BRN2 Is an Androgen Receptor-Suppressed Driver of Neuroendocrine
778 Differentiation in Prostate Cancer. *Cancer Discov* **2017**;7(1):54-71 doi 10.1158/2159-8290.CD-15-
779 1263.
- 780 44. Robinson DR, Wu YM, Vats P, Su F, Lonigro RJ, Cao X, *et al.* Activating ESR1 mutations in
781 hormone-resistant metastatic breast cancer. *Nat Genet* **2013**;45(12):1446-51 doi 10.1038/ng.2823.
- 782 45. Chabon JJ, Simmons AD, Lovejoy AF, Esfahani MS, Newman AM, Haringsma HJ, *et al.* Circulating
783 tumour DNA profiling reveals heterogeneity of EGFR inhibitor resistance mechanisms in lung
784 cancer patients. *Nat Commun* **2016**;7:11815 doi 10.1038/ncomms11815.
- 785 46. Lievre A, Bachet JB, Le Corre D, Boige V, Landi B, Emile JF, *et al.* KRAS mutation status is
786 predictive of response to cetuximab therapy in colorectal cancer. *Cancer Res* **2006**;66(8):3992-5
787 doi 10.1158/0008-5472.CAN-06-0191.
- 788 47. Takeda DY, Spisak S, Seo JH, Bell C, O'Connor E, Korthauer K, *et al.* A Somatic Acquired
789 Enhancer of the Androgen Receptor Is a Noncoding Driver in Advanced Prostate Cancer. *Cell*
790 **2018**;174(2):422-32 e13 doi 10.1016/j.cell.2018.05.037.
- 791 48. Viswanathan SR, Ha G, Hoff AM, Wala JA, Carrot-Zhang J, Whelan CW, *et al.* Structural Alterations
792 Driving Castration-Resistant Prostate Cancer Revealed by Linked-Read Genome Sequencing. *Cell*
793 **2018**;174(2):433-47 e19 doi 10.1016/j.cell.2018.05.036.
- 794 49. Beltran H, Rickman DS, Park K, Chae SS, Sboner A, MacDonald TY, *et al.* Molecular
795 characterization of neuroendocrine prostate cancer and identification of new drug targets. *Cancer*
796 *Discov* **2011**;1(6):487-95 doi 10.1158/2159-8290.CD-11-0130.
- 797 50. Davies AH, Beltran H, Zoubeidi A. Cellular plasticity and the neuroendocrine phenotype in prostate
798 cancer. *Nat Rev Urol* **2018**;15(5):271-86 doi 10.1038/nrurol.2018.22.

- 799 51. Mazrooei P, Kron KJ, Zhu Y, Zhou S, Grillo G, Mehdi T, *et al.* Cistrome Partitioning Reveals
800 Convergence of Somatic Mutations and Risk Variants on Master Transcription Regulators in
801 Primary Prostate Tumors. *Cancer Cell* **2019**;36(6):674-89 e6 doi 10.1016/j.ccell.2019.10.005.
- 802 52. Baca SC, Takeda DY, Seo JH, Hwang J, Ku SY, Arafah R, *et al.* Reprogramming of the FOXA1
803 cistrome in treatment-emergent neuroendocrine prostate cancer. *Nat Commun* **2021**;12(1):1979
804 doi 10.1038/s41467-021-22139-7.
- 805 53. Shafi AA, McNair CM, McCann JJ, Alshalalfa M, Shostak A, Severson TM, *et al.* The circadian
806 cryptochrome, CRY1, is a pro-tumorigenic factor that rhythmically modulates DNA repair. *Nat*
807 *Commun* **2021**;12(1):401 doi 10.1038/s41467-020-20513-5.
- 808 54. Gao S, Chen S, Han D, Wang Z, Li M, Han W, *et al.* Chromatin binding of FOXA1 is promoted by
809 LSD1-mediated demethylation in prostate cancer. *Nat Genet* **2020**;52(10):1011-7 doi
810 10.1038/s41588-020-0681-7.
- 811 55. Gleave ME, Goldenberg SL, Chin JL, Warner J, Saad F, Klotz LH, *et al.* Randomized comparative
812 study of 3 versus 8-month neoadjuvant hormonal therapy before radical prostatectomy:
813 biochemical and pathological effects. *J Urol* **2001**;166(2):500-6; discussion 6-7.
- 814 56. Klotz LH, Goldenberg SL, Jewett MA, Fradet Y, Nam R, Barkin J, *et al.* Long-term followup of a
815 randomized trial of 0 versus 3 months of neoadjuvant androgen ablation before radical
816 prostatectomy. *J Urol* **2003**;170(3):791-4 doi 10.1097/01.ju.0000081404.98273.fd.
- 817 57. Soloway MS, Pareek K, Sharifi R, Wajzman Z, McLeod D, Wood DP, Jr., *et al.* Neoadjuvant
818 androgen ablation before radical prostatectomy in cT2bNxMo prostate cancer: 5-year results. *J*
819 *Urol* **2002**;167(1):112-6.
- 820 58. Singh AA, Schuurman K, Nevedomskaya E, Stelloo S, Linder S, Droog M, *et al.* Optimized ChIP-
821 seq method facilitates transcription factor profiling in human tumors. *Life Sci Alliance*
822 **2019**;2(1):e201800115 doi 10.26508/lsa.201800115.
- 823 59. Schmidt D, Wilson MD, Spyrou C, Brown GD, Hadfield J, Odom DT. ChIP-seq: using high-
824 throughput sequencing to discover protein-DNA interactions. *Methods* **2009**;48(3):240-8 doi
825 10.1016/j.ymeth.2009.03.001.
- 826 60. Li H, Durbin R. Fast and accurate short read alignment with Burrows-Wheeler transform.
827 *Bioinformatics* **2009**;25(14):1754-60 doi 10.1093/bioinformatics/btp324.
- 828 61. Kumar V, Muratani M, Rayan NA, Kraus P, Lufkin T, Ng HH, *et al.* Uniform, optimal signal
829 processing of mapped deep-sequencing data. *Nat Biotechnol* **2013**;31(7):615-22 doi
830 10.1038/nbt.2596.
- 831 62. Zhang Y, Liu T, Meyer CA, Eeckhoute J, Johnson DS, Bernstein BE, *et al.* Model-based analysis
832 of ChIP-Seq (MACS). *Genome Biol* **2008**;9(9):R137 doi 10.1186/gb-2008-9-9-r137.
- 833 63. Ramirez F, Ryan DP, Gruning B, Bhardwaj V, Kilpert F, Richter AS, *et al.* deepTools2: a next
834 generation web server for deep-sequencing data analysis. *Nucleic Acids Res* **2016**;44(W1):W160-
835 5 doi 10.1093/nar/gkw257.
- 836 64. Kharchenko PV, Tolstorukov MY, Park PJ. Design and analysis of ChIP-seq experiments for DNA-
837 binding proteins. *Nat Biotechnol* **2008**;26(12):1351-9 doi 10.1038/nbt.1508.
- 838 65. Li H, Handsaker B, Wysoker A, Fennell T, Ruan J, Homer N, *et al.* The Sequence Alignment/Map
839 format and SAMtools. *Bioinformatics* **2009**;25(16):2078-9 doi 10.1093/bioinformatics/btp352.
- 840 66. Lerdrup M, Johansen JV, Agrawal-Singh S, Hansen K. An interactive environment for agile analysis
841 and visualization of ChIP-sequencing data. *Nat Struct Mol Biol* **2016**;23(4):349-57 doi
842 10.1038/nsmb.3180.
- 843 67. Liu T, Ortiz JA, Taing L, Meyer CA, Lee B, Zhang Y, *et al.* Cistrome: an integrative platform for
844 transcriptional regulation studies. *Genome Biol* **2011**;12(8):R83 doi 10.1186/gb-2011-12-8-r83.

- 845 68. Kuhn RM, Haussler D, Kent WJ. The UCSC genome browser and associated tools. *Brief Bioinform*
846 **2013**;14(2):144-61 doi 10.1093/bib/bbs038.
- 847 69. Ross-Innes CS, Stark R, Teschendorff AE, Holmes KA, Ali HR, Dunning MJ, *et al.* Differential
848 oestrogen receptor binding is associated with clinical outcome in breast cancer. *Nature*
849 **2012**;481(7381):389-93 doi 10.1038/nature10730.
- 850 70. Quinlan AR. BEDTools: The Swiss-Army Tool for Genome Feature Analysis. *Curr Protoc*
851 *Bioinformatics* **2014**;47:11 2 1-34 doi 10.1002/0471250953.bi1112s47.
- 852 71. Gaujoux R, Seoighe C. A flexible R package for nonnegative matrix factorization. *BMC*
853 *Bioinformatics* **2010**;11:367 doi 10.1186/1471-2105-11-367.
- 854 72. Subramanian A, Tamayo P, Mootha VK, Mukherjee S, Ebert BL, Gillette MA, *et al.* Gene set
855 enrichment analysis: a knowledge-based approach for interpreting genome-wide expression
856 profiles. *Proc Natl Acad Sci U S A* **2005**;102(43):15545-50 doi 10.1073/pnas.0506580102.
- 857 73. Kim D, Pertea G, Trapnell C, Pimentel H, Kelley R, Salzberg SL. TopHat2: accurate alignment of
858 transcriptomes in the presence of insertions, deletions and gene fusions. *Genome Biol*
859 **2013**;14(4):R36 doi 10.1186/gb-2013-14-4-r36.
- 860 74. Anders S, Pyl PT, Huber W. HTSeq--a Python framework to work with high-throughput sequencing
861 data. *Bioinformatics* **2015**;31(2):166-9 doi 10.1093/bioinformatics/btu638.
- 862 75. Love MI, Huber W, Anders S. Moderated estimation of fold change and dispersion for RNA-seq
863 data with DESeq2. *Genome Biol* **2014**;15(12):550 doi 10.1186/s13059-014-0550-8.
- 864 76. Consortium EP. An integrated encyclopedia of DNA elements in the human genome. *Nature*
865 **2012**;489(7414):57-74 doi 10.1038/nature11247.
- 866 77. Ho D, Imai K, King G, Stuart EA. MatchIt: Nonparametric Preprocessing for Parametric Causal
867 Inference. 2011 **2011**;42(8):28 doi 10.18637/jss.v042.i08.
- 868

869 **Tables**

870 **Table 1: Characteristics of the DARANA cohort (n=56).**

871 Table summarizing the patient baseline demographics, and pre- and post-treatment disease characteristics of the DARANA cohort.
 872 Shown are age (years), initial Prostate-specific antigen (PSA) serum levels (ng/mL) and International Society of Urological Pathology
 873 (ISUP) grade at diagnosis (with associated Gleason scores (GS)). In addition, T-stage (T) and Lymph node status (N) before (pre =
 874 at diagnosis) and after (post = at surgery) neoadjuvant ENZ therapy, as well as the surgical margin status of the prostatectomy
 875 specimens are shown. Pre-treatment measures are based on histological evaluation of biopsy material and radiographic evaluation
 876 (clinical grading; c), while post-treatment assessments are based on histological evaluations of prostatectomy specimens (pathological
 877 grading after neoadjuvant therapy; yp). Biochemical recurrence (BCR) was defined as a rise in PSA of ≥ 0.2 ng/mL. Mean time to
 878 BCR (months) and time to last follow-up (months) are indicated. For continuous variables (age, baseline PSA, time to BCR, and time
 879 to last follow-up) the mean and 95% confidence interval (CI) are shown. For categorical variables (baseline ISUP, T-stage, N-status,
 880 surgical margins, BCR) the number of patients (no.) and percentages (%) are indicated.

DARANA cohort (n= 56)		
Age – years (95% CI)	67 (65-68)	
Baseline PSA level – ng/mL (95% CI)	12.8 (10.4-15.2)	
Baseline ISUP grade – no. (%)		
ISUP 1 (GS 3+3)	0 (0)	
ISUP 2 (GS 3+4)	16 (28)	
ISUP 3 (GS 4+3)	9 (16)	
ISUP 4 (GS 4+4, 3+5, 5+3)	20 (36)	
ISUP 5 (GS 4+5, 5+4, 5+5)	11 (20)	
T-stage (T) – no. (%)	Pre (cT)	Post (ypT)
T1	1 (2)	/
T2	25 (44)	20 (36)
T3	29 (52)	36 (64)
T4	1 (2)	0 (0)
Lymph node status (N) – no. (%)	Pre (cN)	Post (ypN)
N0	53 (95)	39 (70)
N1	3 (5)	17 (30)
Surgical margins – no. (%)		
Negative	39 (70)	

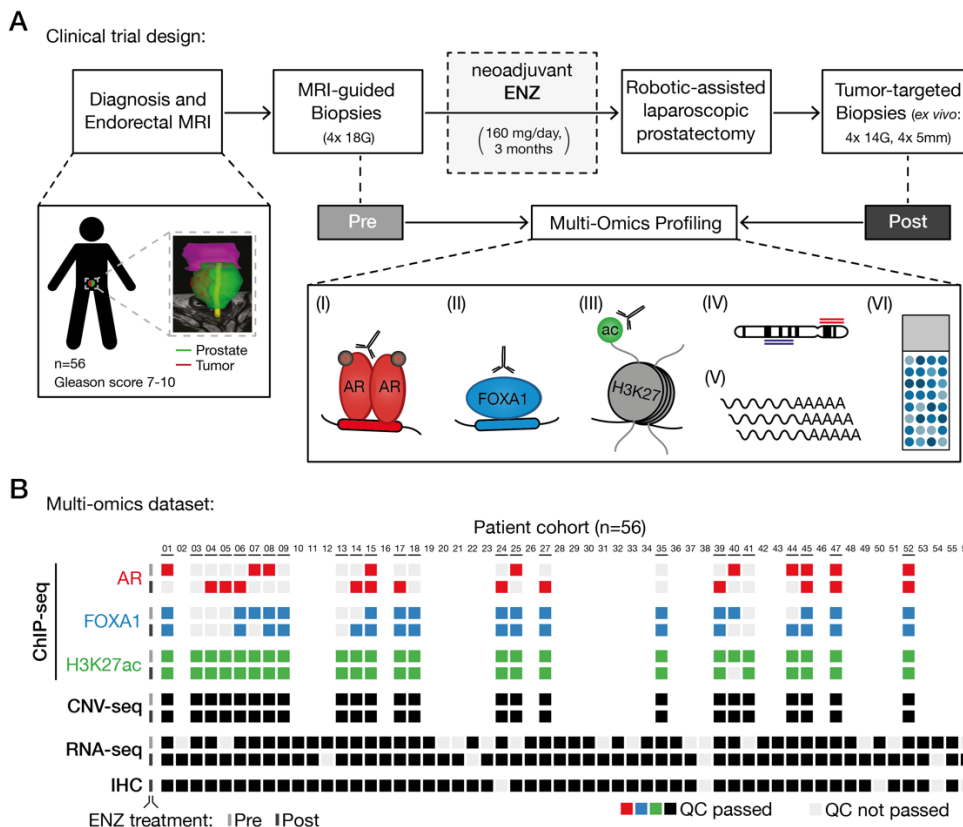
Positive	17 (30)
Biochemical recurrence (BCR) – no. (%)	PSA \geq 0.2 ng/mL
No	32 (57)
Yes	23 (41)
Unknown	1 (2)
Mean time to BCR – months (95% CI)	12 (8-15)
Mean time to last follow-up – months (95% CI)	37 (33-42)

881

882

883 **Figures**

Figure 1



884

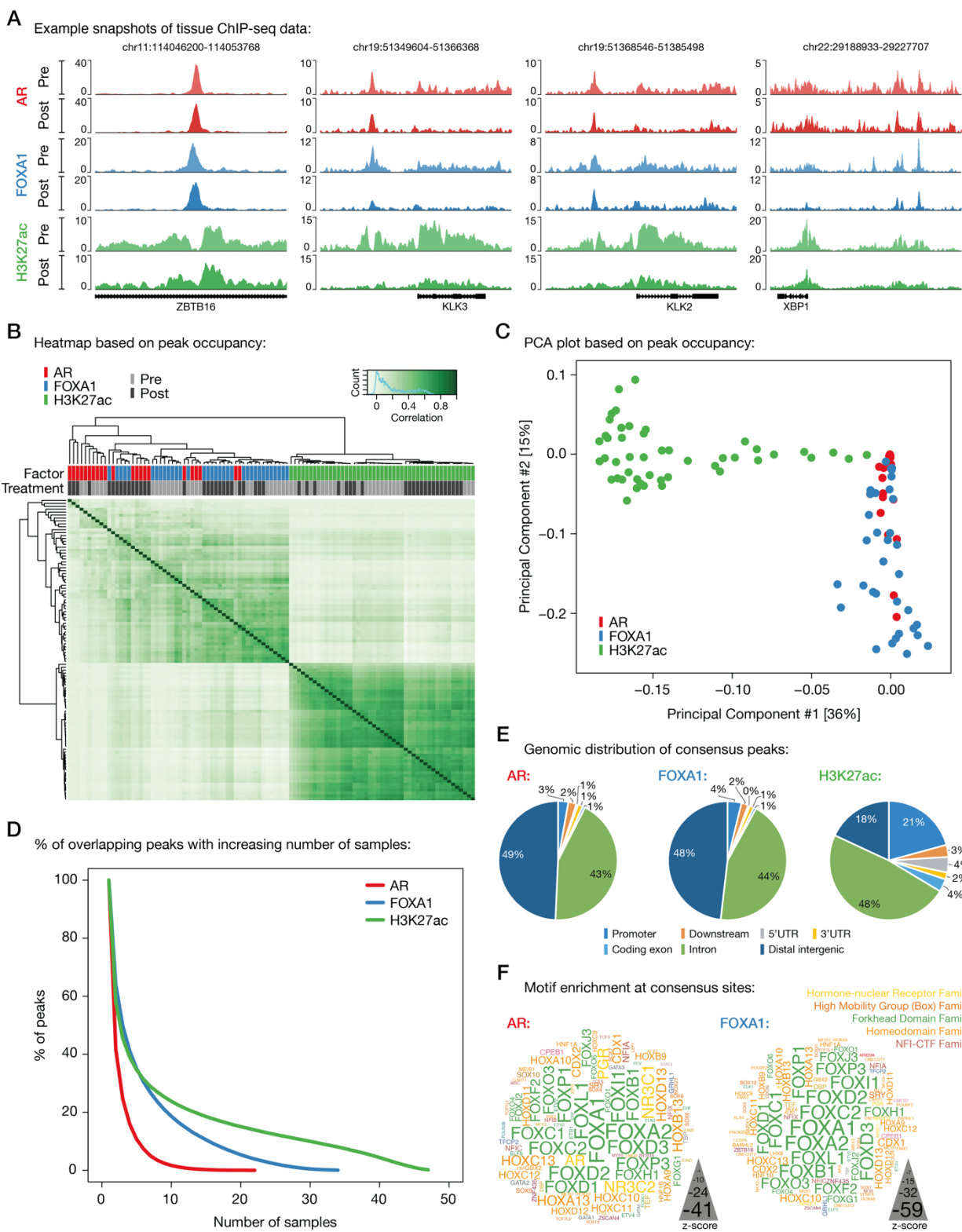
885 **Figure 1: Clinical trial design and omics data sample collection.**

886 (A) Study design of the DARANA trial (NCT03297385). Multi-omics profiling, consisting of (I) Androgen Receptor (AR) ChIP-
 887 seq, (II) FOXA1 ChIP-seq, (III) H3K27ac ChIP-seq, (IV) DNA copy number sequencing (CNV-seq), (V) gene expression
 888 profiling (RNA-seq) and (VI) immunohistochemistry (IHC) analysis, was performed on MRI-guided biopsy samples prior
 889 to ENZ treatment (Pre) and tumor-target prostatectomy specimens after 3 months of neoadjuvant ENZ therapy (Post).

890 (B) Overview of data availability and quality control analyses for each sample. Individual data streams are indicated
 891 separately with ChIP-seq for AR (red), FOXA1 (blue), H3K27ac (green), CNV-seq, RNA-seq and IHC (all black). The
 892 ENZ treatment status indicates the pre-treatment (top) and post-treatment samples (bottom) per omics dataset. Samples
 893 not passing QC (light gray) were successfully applied for focused raw data analyses. Blank spots for ChIP-seq or CNV-
 894 seq samples indicate that the fresh-frozen material didn't pass the tumor cell percentage cut-off of $\geq 50\%$.

895

Figure 2



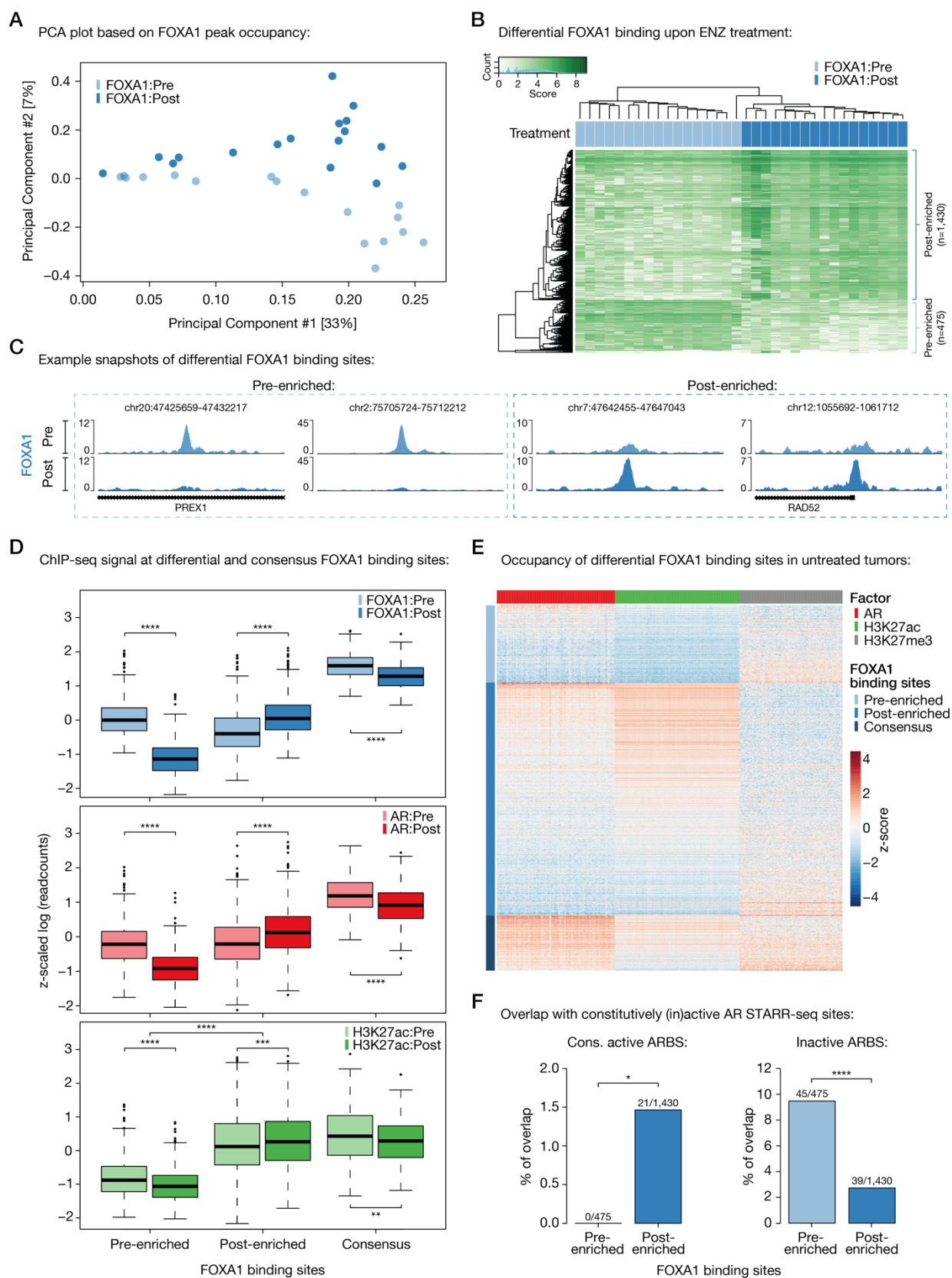
896

897

Figure 2: Characterization of tissue ChIP-seq data streams.

- 898 (A) Representative example snapshots of AR (red), FOXA1 (blue) and H3K27ac (green) ChIP-seq data for four genomic
899 loci in one patient. Pre- (light colors) and post-ENZ treatment (dark colors) is indicated. Y-axis indicates ChIP-seq
900 signal in fragments per kilobase per million reads mapped (FPKM).
- 901 (B) Correlation heatmap based on peak occupancy. Clustering of the samples is based on all called peaks and
902 represents Pearson correlations between individual ChIP-seq samples. The column color bars indicate the ChIP-seq
903 factor (AR, FOXA1, H3K27ac) and treatment status (Pre, Post).
- 904 (C) Principal component analysis (PCA) plot based on peak occupancy. Each dot represents a ChIP-seq sample that is
905 colored per factor.
- 906 (D) Elbow plot depicting the peak overlap between ChIP-seq samples per factor. Shown is the percentage of overlapping
907 peaks with increasing number of samples. Consensus peaksets were designed by using a cut-off of peaks present
908 in at least 3 AR, 7 FOXA1, or 13 H3K27ac samples.
- 909 (E) Pie charts showing the genomic distribution of AR (left), FOXA1 (middle) and H3K27ac (right) consensus peaks.
- 910 (F) Word clouds show motif enrichment at AR (left) and FOXA1 (right) consensus sites. The font size represents the z-
911 score and colors correspond to transcription factor families.
- 912

Figure 3

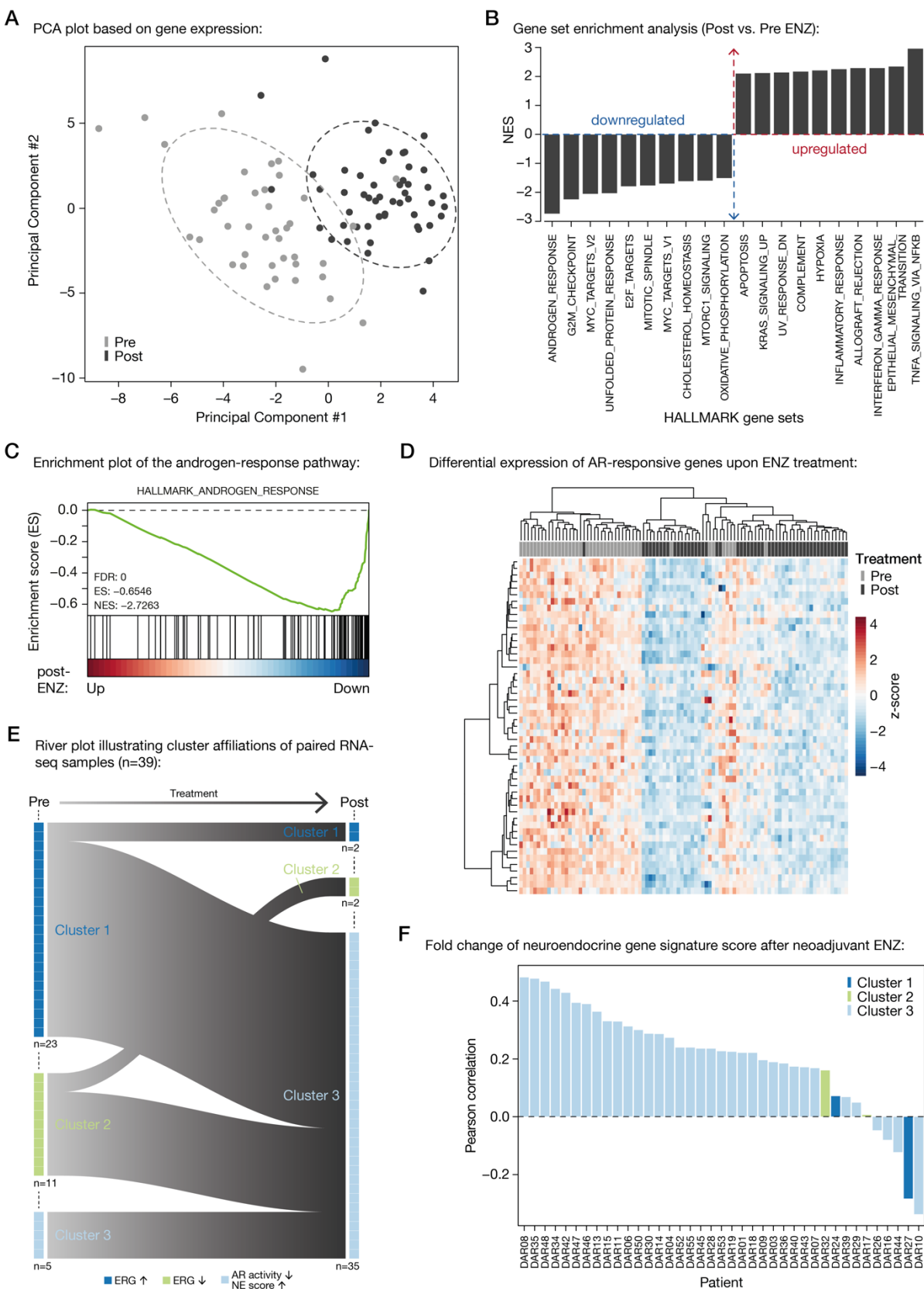


914 **Figure 3: Differential FOXA1 binding upon ENZ treatment.**

- 915 (A) Principle component analysis (PCA) plot based on peak occupancy of FOXA1 ChIP-seq data. Color indicates pre-
916 treatment (light blue) and post-treatment (dark blue) FOXA1 samples.
- 917 (B) Coverage heatmap depicting differential FOXA1 binding sites, selectively enriched in the pre-treatment (n=475) or post-
918 treatment (n=1,430) setting.
- 919 (C) Representative example snapshots of FOXA1 ChIP-seq signal at two pre-enriched (left) and two post-enriched (right)
920 FOXA1 sites in one patient. Pre- (light blue) and post-ENZ treatment (dark blue) is indicated. Y-axis indicates ChIP-seq
921 signal in FPKM.
- 922 (D) Boxplots indicating ChIP-seq signal (z-scaled readcounts) at pre-enriched (n=475), post-enriched (n=1,430) and
923 consensus FOXA1 peaks (shared by ≥ 30 patients; n=338) for FOXA1 (blue), AR (red), and H3K27ac (green) ChIP-seq
924 datasets before (Pre; light colors) and after (Post; dark colors) ENZ treatment. **, $P < 0.01$; ***, $P < 0.001$; ****, $P <$
925 0.0001 (Mann-Whitney U-test adjusted for multiple testing using FDR).
- 926 (E) Coverage heatmap showing occupancy of differential (pre-/post-enriched) and consensus FOXA1 peaks in an external
927 ChIP-seq dataset consisting of 100 untreated primary tumors (31). Heatmap color indicates region read counts (z-score)
928 at pre-enriched, post-enriched and consensus FOXA1 sites (rows) in the AR (red), H3K27ac (green) and H3K27me3
929 (gray) ChIP-seq data streams (columns).
- 930 (F) Bar chart representing the overlap between differential FOXA1 sites (pre-enriched or post-enriched) and constitutively
931 active (left) or inactive (right) AR binding sites (ARBS), based on STARR-seq. *, $P < 0.05$; ****, $P < 0.0001$ (Fisher's
932 exact test).

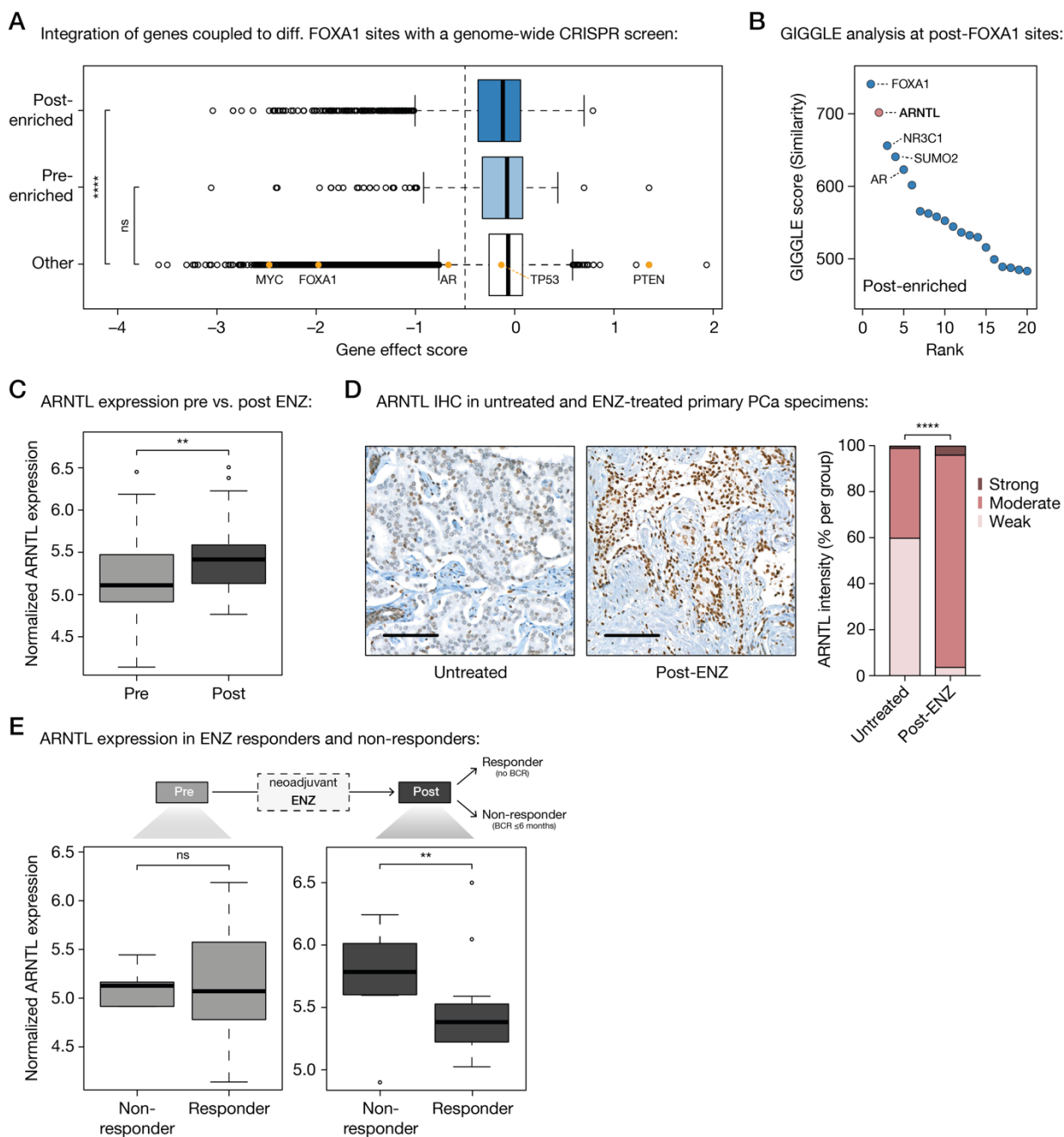
933

Figure 4



- 935 **Figure 4: Neoadjuvant ENZ deactivates AR signaling and induces neuroendocrine (NE)-like gene expression signatures.**
- 936 (A) Principle component analysis (PCA) plot based on gene expression data. Color indicates pre-treatment (gray) and post-
- 937 treatment (black) samples. Ellipses are based on the 80% confidence interval.
- 938 (B) Gene set enrichment analyses (GSEA) for Hallmark gene sets. Shown are the top differentially enriched pathways upon
- 939 ENZ treatment. Y-axis indicates the normalized enrichment score (NES).
- 940 (C) Enrichment plot of the Hallmark Androgen Response pathway, for genes up- or downregulated after ENZ. Y-axis
- 941 indicates enrichment score (ES). GSEA statistics (FDR, ES, NES) are indicated.
- 942 (D) Unsupervised hierarchical clustering of pre- and post-treatment RNA-seq samples based on the expression of AR-
- 943 responsive genes. Color scale indicates gene expression (z-score).
- 944 (E) River plot showing state transitions between Clusters 1 (dark blue), Cluster 2 (green) and Cluster 3 (light blue) for paired
- 945 pre-treatment and post-treatment RNA-seq samples (n=39). Number of samples assigned to each cluster before and
- 946 after treatment as well as the hallmarks per cluster are indicated.
- 947 (F) Waterfall plot depicting the Pearson correlation of neuroendocrine gene expression signature fold changes upon ENZ
- 948 treatment per patient. Colors indicate the patients cluster affiliations after treatment.
- 949

Figure 5



950

951 **Figure 5: Acquired FOXA1 sites drive key-survival genes that are under control of circadian rhythm regulator ARNTL.**

952 (A) Boxplot showing DepMap (20Q1) genome-wide loss-of-function CRISPR screen data for VCaP PCa cells, separately
 953 analyzing the gene effect score of genes associated with post-enriched FOXA1 sites (top), pre-enriched FOXA1 sites
 954 (middle) or all other tested genes (bottom). Differential FOXA1 binding sites were coupled to their respective target genes
 955 using H3K27ac HiChIP data. Indicated as controls are PCa-relevant driver genes: oncogenes *MYC*, *FOXA1*, *AR*, *TP53*

956 and tumor suppressor *PTEN*. The recommended gene effect score cutoff of -0.5 is shown (dotted vertical line). ns, $P >$
957 0.05; ****, $P < 0.0001$ (Fisher's exact test).

958 (B) Dot plot representing ranked GIGGLE similarity scores for transcriptional regulators identified at post-treatment FOXA1
959 sites. The top 20 factors identified are shown, and the 5 most enriched factors are labeled.

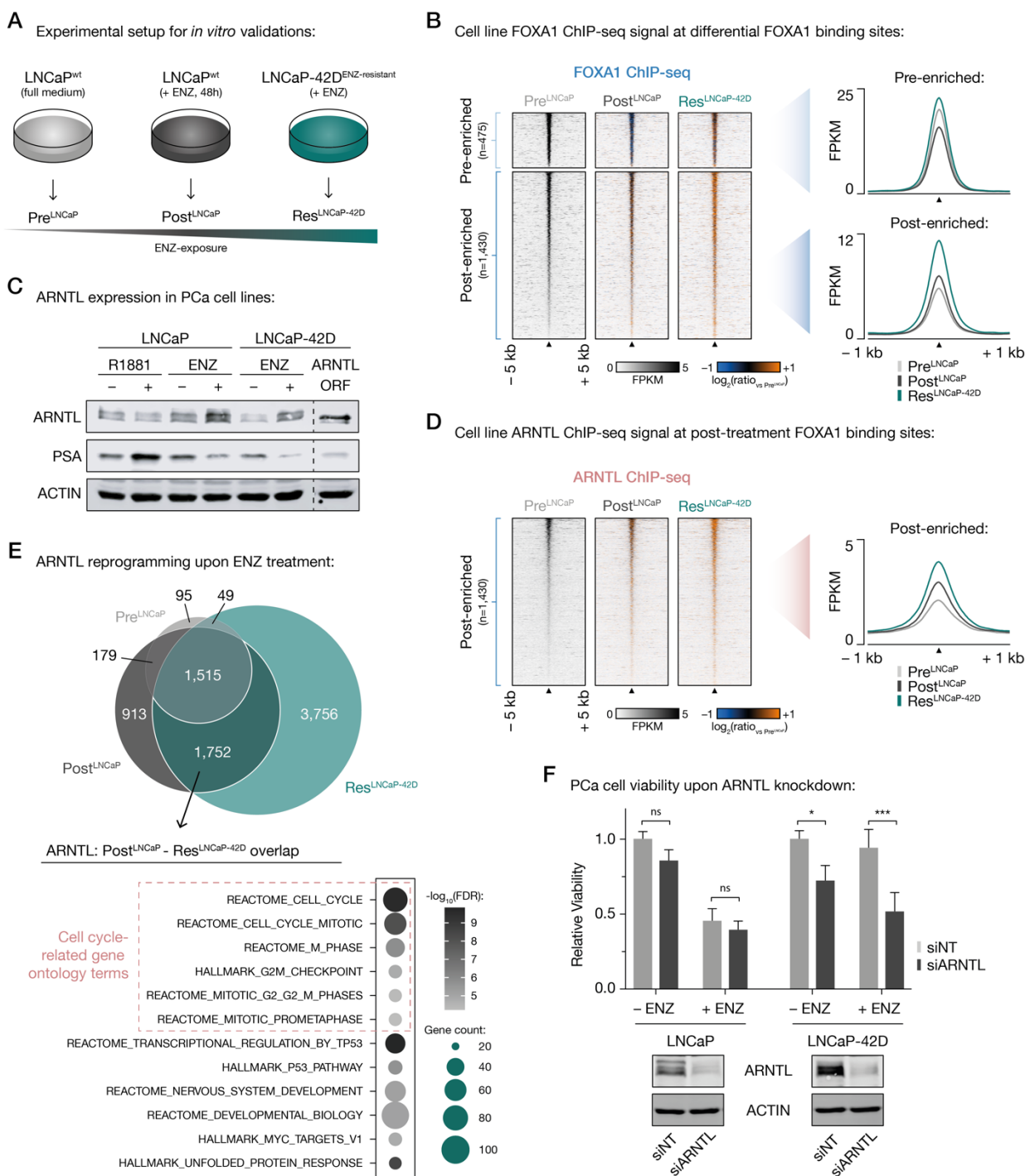
960 (C) Boxplot showing normalized ARNTL gene expression before and after 3 months of neoadjuvant ENZ treatment. **, $P <$
961 0.01 (Mann-Whitney U-test).

962 (D) Representative ARNTL immunohistochemistry (IHC) stainings (left) and quantification of ARNTL staining intensity (right)
963 in tissue microarrays consisting of prostatectomy specimens from untreated patients (not receiving neoadjuvant ENZ;
964 $n=110$) and DARANA patients post-ENZ ($n=51$). Scale bars, 100 μm . ****, $P < 0.0001$ (Fisher's exact test).

965 (E) Boxplots depicting normalized ARNTL gene expression in ENZ non-responders (biochemical recurrence (BCR) ≤ 6
966 months; $n=8$) and responders (no BCR; $n=29$) in the pre- (left) and post- (right) treatment setting separately. ns, $P > 0.05$;
967 **, $P < 0.01$ (Mann-Whitney U-test).

968

Figure 6



969

970 **Figure 6: Treatment-induced dependency on ARNTL in ENZ-resistant PCa cells.**

971 (A) Experimental setup for *in vitro* validation experiments.

972 (B) Tornado plots (left) and average density plots (right) visualizing FOXA1 ChIP-seq signal (in FPKM) at pre-enriched (top)

973 and post-enriched (bottom) FOXA1 binding sites in untreated (Pre^{LNCaP}), short-term ENZ-treated (Post^{LNCaP}), and ENZ-

974 resistant NE-like LNCaP cells (Res^{LNCaP-42D}). Data are centered at differential FOXA1 peaks depicting a 5-kb (heatmaps)
975 or 1-kb (density plots) window around the peak center. Heatmap color depicts the ChIP-seq signal compared to the
976 untreated condition (Pre^{LNCaP}), with blue indicating lower peak intensity and orange indicating higher peak intensity.
977 Average of two biological replicates is represented.

978 (C) Western blot showing ARNTL protein levels in LNCaP and LNCaP-42D cells following treatment with synthetic androgen
979 (R1881) and/or ENZ (ENZ) for 48 h. ARNTL overexpression (in LNCaP-42D cells) as well as stainings for PSA and
980 ACTIN are included as controls for antibody staining, hormonal treatment and protein loading, respectively. Images are
981 representative of three independent experiments.

982 (D) Tornado plots (left) and average density plot (right) visualizing ARNTL ChIP-seq signal (in FPKM) at post-enriched
983 FOXA1 binding sites in untreated (Pre^{LNCaP}), short-term ENZ-treated (Post^{LNCaP}), and ENZ-resistant NE-like LNCaP cells
984 (Res^{LNCaP-42D}). Data are centered at post-treatment FOXA1 peaks depicting a 5-kb (heatmaps) or 1-kb (density plots)
985 window around the peak center. Heatmap color depicts the ChIP-seq signal compared to the untreated condition
986 (Pre^{LNCaP}), with blue indicating lower peak intensity and orange indicating higher peak intensity. Average of two biological
987 replicates is represented.

988 (E) Venn diagram (top) indicating the overlap of ARNTL binding sites in all tested cell line conditions (Pre^{LNCaP}, Post^{LNCaP},
989 Res^{LNCaP-42D}). For each condition, only peaks present in both replicates were included. Gene ontology terms for ARNTL-
990 bound gene sets uniquely shared between Post^{LNCaP} and Res^{LNCaP-42D} conditions are presented below. Overlapping
991 ARNTL binding sites (n=1,752) were coupled to their respective target genes using H3K27ac HiChIP data. Color
992 indicates the gene set enrichment (FDR q-value) and size depicts the number of genes that overlap with the indicated
993 gene sets. Cell cycle-related gene ontology terms are highlighted.

994 (F) Bar chart (top) showing relative cell viability of LNCaP (left) and LNCaP-42D (right) cells upon transfection with non-
995 targeting siRNA (siNT) or siARNTL, and exposure to ENZ. Cell viability assays were performed 7 days post-transfection.
996 ENZ treatment is indicated and the average of three biological replicates is shown relative to the untreated (– ENZ) siNT
997 condition per cell line. Western blots (bottom) indicate ARNTL protein levels in LNCaP (left) and LNCaP-42D (right) cells
998 following siRNA-mediated silencing of ARNTL for 48 h. Transfection with siNT and staining for ACTIN are included as
999 controls for siRNA treatment and protein loading, respectively. Images are representative of three independent
1000 experiments. ns, $P > 0.05$; *, $P < 0.05$; ***, $P < 0.001$ (two-way ANOVA followed by Tukey's multiple comparisons test).
1001